

Master's Thesis

**A Study of Dark Matter at Electron-Positron
Colliders using High Performance Computing**

Kihong Park

Data & High Performance Computing Science

UNIVERSITY OF SCIENCE AND TECHNOLOGY

August 2021

A Study of Dark Matter at Electron-Positron Colliders using High Performance Computing 2021 Kihong Park

**A Study of Dark Matter at Electron-Positron
Colliders using High Performance Computing**

Supervisor Kihyeon Cho

**A Dissertation Submitted in Partial Fulfillment of Requirements
For the Degree of Master**

August 2021

**UNIVERSITY OF SCIENCE AND TECHNOLOGY
Major of Data & High Performance Computing Science**

Kihong Park

**We hereby approve the M.S.
thesis of “Kihong Park”.**

August 2021

Prof. Minjoong Jeong **sign**

Chairman of Thesis Committee

Prof. Hongsuk Yi **sign**

Thesis Committee Member

Prof. Kihyeon Cho **sign**

Thesis Committee Member

UNIVERSITY OF SCIENCE AND TECHNOLOGY

ABSTRACT

Even if the Standard Model (SM) describing particles that constitutes the universe and its interactions is well established, the SM cannot explain dark matter. Therefore, little is known about dark matter and is being explored by various means. In this thesis, we study dark matter at electron-positron collider experiments using toolkits utilized in particle collider experiments. The signal channel is $e^+ e^- \rightarrow \mu^+ \mu^- A'$ with $A' \rightarrow \mu^+ \mu^-$ and the theoretical model is the simplified model. We investigated the dependence of cross-section according to various parameters. Ultimately, we obtained detector acceptance for the signal channel in present and/or future electron-positron collision experiments. In addition, we used the KIST-5 supercomputer and a local machine to compare central processing unit time of simulation. It has been confirmed that the high efficiency of parallel processing of supercomputers and the many number of cores can be utilized to increase the efficiency of dark matter research. The results of this study will help to find dark matter signals for the signal channel in present and/or future electron-positron collider experiments such as Belle II, Future Circular Collider (FCC)-ee, Circular Electron-Positron Collider (CEPC), and International Linear Collider (ILC).

Keywords : Dark matter, Dark photon, High energy physics, Electron-positron collider, Computational science, High performance computing

국문 초록

우주를 구성하는 물질과 그 상호작용을 기술하는 표준모형은 잘 확립되었지만 암흑물질에 대하여 설명할 수 없다. 따라서 암흑물질에 관하여 알려진 바는 적고 여러 가지 수단으로 탐색 중에 있다. 본 학위논문에서는 입자충돌실험 연구에 활용되는 여러 가지 툴킷을 활용하여 전자-양전자 충돌실험에서 암흑물질을 연구한다. 신호사건은 $e^+ e^- \rightarrow \mu^+ \mu^- A'$ with $A' \rightarrow \mu^+ \mu^-$ 이고 이론적 모델은 simplified model 이다. 여러 가지 매개변수에 따른 산란단면적을 조사하였다. 궁극적으로 현재 및 미래의 전자-양전자 충돌실험에서의 신호사건에 대한 검출기 수용율을 구하였다. 또한 KISTI 슈퍼컴퓨터 5 호기 및 로컬머신을 활용하여 모의시뮬의 중앙처리장치(CPU) 시간을 비교하였다. 슈퍼컴퓨터의 높은 병렬처리효율과 많은 코어 수를 활용하여 암흑물질 연구 효율을 높일 수 있음을 확인할 수 있었다. 이 연구의 결과는 Belle II, FCC-ee, CEPC 그리고 ILC 등의 현재 및 미래의 전자-양전자 충돌실험에서 본 연구의 신호사건에 대한 암흑물질 신호를 찾는 데 도움이 될 것이다.

주요단어(Key words): 암흑물질, 암흑광자, 고에너지물리, 전자-양전자 충돌기, 계산과학, 고성능컴퓨팅

Contents

1. Introduction.....	1
2. Theory.....	3
2.1 Signal channel of $e + e \rightarrow \mu + \mu - A'$ with $A' \rightarrow \mu + \mu -$	3
2.2 The simplified model	4
3. Methods	13
4. Results.....	18
4.1 Background study using the standard model.....	18
4.2 Signal channel studies based on the stand-alone frame	27
4.2.1 Studies at generation level	27
4.2.2 Studies at reconstruction level.....	34
4.3 Signal channel studies based on the basf2	61
4.4 CPU time studies on machines.....	66
5. Conclusion	74

List of Figures

Figure 1. Diagram showing interactions between the SM and dark sector.....	3
Figure 2. Feynman diagram of the simplified model at a hadron collider.	4
Figure 3. Feynman diagram of the simplified model at a lepton collider.....	5
Figure 4. Feynman diagrams of $p p \rightarrow \chi d \chi d$ with spin 1.....	6
Figure 5. Feynman diagrams of $p p \rightarrow \chi d \chi d \gamma$ with spin 0.....	7
Figure 6. Feynman diagrams of $p p \rightarrow \chi d \chi d \gamma$ with spin 1.....	8
Figure 7. Feynman diagrams of $e + e \rightarrow \chi d \chi d \gamma$ with spin 0.....	10
Figure 8. Feynman diagram illustrating the coupling constants.	11
Figure 9. The flowcharts of the stand-alone frame (left) and the basf2 (right).	14
Figure 10. Standard model (SM) cross-section for different center of mass (CM) energies.	19
Figure 11. The Feynman diagrams of dominant modes of the standard model.	20
Figure 12. Total 48 Feynman diagrams of background process.	21
Figure 13. The possible Feynman diagrams of the signal mode.....	28
Figure 14. Cross-section dependence on the center of mass (CM) energy.	30
Figure 15. Cross-section dependence on the mass of dark photon.	31
Figure 16. Cross-section dependence on the coupling constant.	32
Figure 17. Cross-section dependence on the CM energy varying the mass of dark photon.	33
Figure 18. Comparison of generation level and reconstruction level at the Belle II (10.58 GeV). Number of events (y-axis) are multiplied by cross-section (40.6 pb).....	36
Figure 19. Comparison of generation level and reconstruction level at the FCC-ee (91 GeV). Number of events (y-axis) are multiplied by cross-section (292 pb).....	40
Figure 20. Comparison of generation level and reconstruction level at the FCC-ee (160 GeV). Number of events (y-axis) are multiplied by cross-section (4.88 pb).....	44
Figure 21. Comparison of generation level and reconstruction level at the CEPC (160 GeV). Number of events (y-axis) are multiplied by cross-section (4.88 pb).....	48
Figure 22. Comparison of generation level and reconstruction level at the CEPC (240 GeV). Number of events (y-axis) are multiplied by cross-section (2.0 pb).....	52
Figure 23. Comparison of generation level and reconstruction level at the ILC (500 GeV). Number of events (y-axis) are multiplied by cross-section (0.463 pb).....	56
Figure 24. Detector acceptance of experiments.	60
Figure 25. Feynman diagrams of the signal process.....	62

Figure 26. Comparison of generation level and reconstruction based on the stand-alone frame. Number of events (y-axis) are multiplied by cross-section (40.6 pb).	64
Figure 27. Comparison of generation level and reconstruction based on basf2. Number of events (y-axis) are multiplied by cross-section (35.4 pb).....	65
Figure 28. Flowchart of the physics and full simulation.	68
Figure 29. Wall-clock time with one core or 15 cores on machines with physics simulation only.	71
Figure 30. Speed up on machines and ideal case.	71
Figure 31. Wall-clock time with one core on machines with the full simulation.	72
Figure 32. Wall-clock time as the number of jobs increases for different machines.....	73

List of Tables

Table 1. The possible or impossible process according to spin.	5
Table 2. Identification of the coupling constants.	11
Table 3. Parameters of the present and/or future electron-positron colliders ((Zyla P. A., et al 2020)).	12
Table 4. Parameters of the stand-alone frame and the basf2.	14
Table 5. Software, input file, and output file of processing based on the stand-alone frame.	15
Table 6. Software, code file, input file, and output file of processing based on the basf2.	16
Table 7. The specification of the machine used in the stand-alone frame and the basf2..	17
Table 8. The settings for the standard model (SM) event generation.	19
Table 9. The settings for the signal event generation.	27
Table 10. Primary/secondary mediator of the signal process.	29
Table 11. The settings for reconstruction level study.	34
Table 12. CM energy, signal process, Delphes η cut, Delphes card on e+ e- collider experiments.	35
Table 13. Detector acceptance of experiments.	60
Table 14. The settings for the signal event generation based on the basf2.	61
Table 15. Parameters and detector acceptance of the stand-alone frame and the basf2....	63
Table 16. The specification of the KISTI-5 supercomputer and the local Linux machine.	67
Table 17. The configuration for the three cases.	69

Abbreviations

Abbreviation	Explanation
bsasf2	Belle II Analysis Software Framework
CEPC	Circular Electron-Positron Collider
CM	Center of Mass
CPU	Central Processing Unit
DM	Dark Matter
EFT	Effective Field Theory
FCC	Future Circular Collider
HEP	High Energy Physics
HPC	High Performance Computing
ILC	International Linear Collider
KNL	Knights Landing
SKL	Skylake
SM	Standard Model
SUSY	Supersymmetry
UV theory	Ultraviolet theory

1. Introduction

The standard model (SM) of particle physics successfully describes fundamental particles and their interactions. Dark matter accounts for 26 percent of the universe's density, but the SM does not explain what dark matter is. Theorists, therefore, present many dark matter candidates in beyond the SM (Cho 2016a). There are three ways to search for dark matter: direct detection, indirect detection, particle collider detection (Cho 2016b; Cho 2017). Particle colliders include hadronic collider and leptonic collider. Lepton collider has the advantage of giving a clearer signal and lower background than hadronic collider (Cho 2017). In this thesis, we studied dark matter at lepton collider, especially electron-positron colliders. The ongoing electron-positron collider experiments include Belle II, and the future experiments include Future Circular Collider (FCC)-ee, Circular Electron-Positron Collider (CEPC), and International Linear Collider (ILC). We used a high energy physics (HEP) simulation toolkits to scan energies of present and/or future collider experiments and obtain detector acceptance on each experiments (Alwall et al. 2014; Yeo & Cho 2018). For this study, we choose a signal channel in which dark photons couple only to heavy leptons (Shuve & Yavin 2014; Yeo & Cho 2018). The reason for choosing the signal channel is that this theory can explain the muon anomalous magnetic moment (Yeo & Cho 2018). We only dealt with dark photons decaying into two muons using the simplified model (Alves et al. 2012).

The cross-section of dark matter is a thousand times smaller than that of the SM particles. In addition, there are large parameter areas that need to be explored.

This requires a large amount of simulation and thus consumes much central processing unit (CPU) time. Therefore, it is essential to optimize CPU time to increase the efficiency of dark matter research. To help to optimize CPU time, we studied the CPU time of simulation using the KISTI-5 supercomputer (Knights Landing (KNL) and Skylake (SKL)) and a local Linux machine.

2. Theory

2.1 Signal channel of $e^+e^- \rightarrow \mu^+\mu^-A'$ with $A' \rightarrow \mu^+\mu^-$

We assume that the SM and the dark sector interact with each other via γ (photon) and A' (dark photon) mixing, as shown in Figure 1. If dark photons in the dark sector interact with the particles of SM, the dark photon can be coupled with charged lepton, muon, which corresponds to dark sector type 4 (Yeo, I., & Cho, K. ,2018; Shuve, B., & Yavin, I. ,2014). The signal process is $e^+e^- \rightarrow \mu^+\mu^-A'$ with a dark photon $A' \rightarrow \mu^+\mu^-$. This theory has the advantage of explaining the muon anomalous magnetic moment (Shuve, B., & Yavin, I. ,2014). If the mass of dark photon is less than the masses of the two muons, the dark photon decays into two neutrinos or two dark matter particles. These become Missing Transverse Energy (MET) without leaving a trace on the detector. For dark photons to decay into two muons, the mass of dark photons must be greater than 211.32 MeV, which is the mass of two muons. In the study, dark photons were considered spin 1 since dark photon is regarded as vector boson.

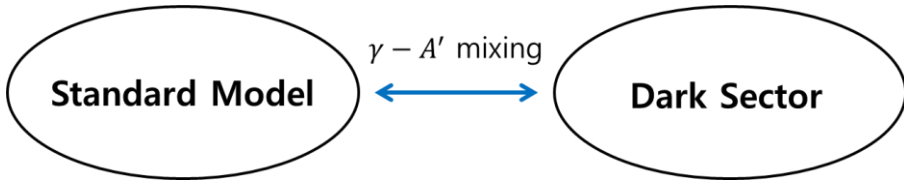


Figure 1. Diagram showing interactions between the SM and dark sector.

2.2 The simplified model

The theoretical model of this study is the simplified Model (Alves, D., et al. ,2012). This is simplified dark matter models for next leading order (NLO). This model consists of different types of dark matter and different types of mediators. The mass of dark matter and the mass of dark photon can be changed in the parameter card (param_card.dat). Figure 2 shows the Feynman diagram of the simplified model at a hadron collider. The simplified model includes SM particles and dark matter particles, and mediator particles, that is, dark photon. This model is placed between the ultraviolet (UV) model and effective field theory. The UV model includes supersymmetry (SUSY) particles and extra dimensions, while the effective field theory includes SM and dark matter particles. The simplified model was imported in MadGraph5 when generating signal events. This model can be downloaded from the following website:

<http://feynrules.irmp.ucl.ac.be/wiki/DMSimp#no1>.

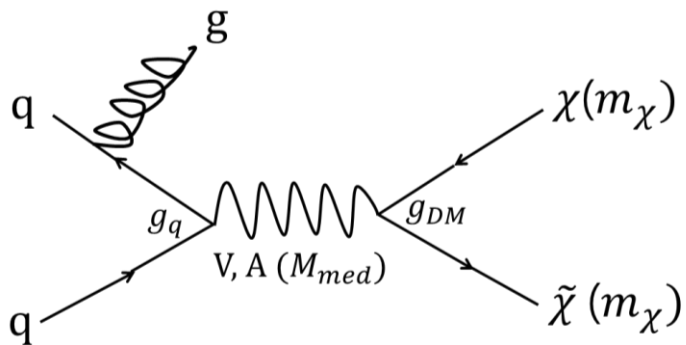


Figure 2. Feynman diagram of the simplified model at a hadron collider.

This model can be used for electron-positron collider simulation as well as proton-proton collider simulation. Figure 3 shows the Feynman diagram of the simplified model at a lepton collider. Table 1 shows the possible or impossible processes according to spin. χ_d ($\tilde{\chi}_d$) denotes the Dirac spinor dark matter (anti-dark matter).

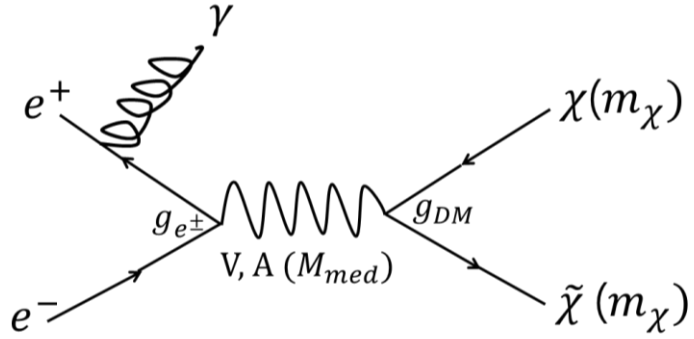


Figure 3. Feynman diagram of the simplified model at a lepton collider.

Table 1. The possible or impossible process according to spin.

Process	Code	spin 0	spin 1
$p p \rightarrow \chi_a \tilde{\chi}_a$	p p > xd xd~	-	14 diagrams
$p p \rightarrow \chi_a \tilde{\chi}_a \gamma$	p p > xd xd~ a	20 diagrams	28 diagrams
$e^+ e^- \rightarrow \chi_a \tilde{\chi}_a$	e+ e-> xd xd~	-	-
$e^+ e^- \rightarrow \chi_a \tilde{\chi}_a \gamma$	e+ e-> xd xd~ a	2 diagrams	-

(1) $p p \rightarrow \chi_d \widetilde{\chi}_d$ (spin 1) total 14 diagrams (7 independent)

Figure 4 shows the Feynman diagrams of $p p \rightarrow \chi_d \widetilde{\chi}_d$ with spin 1. It shows the 7 independent Feynman diagrams.

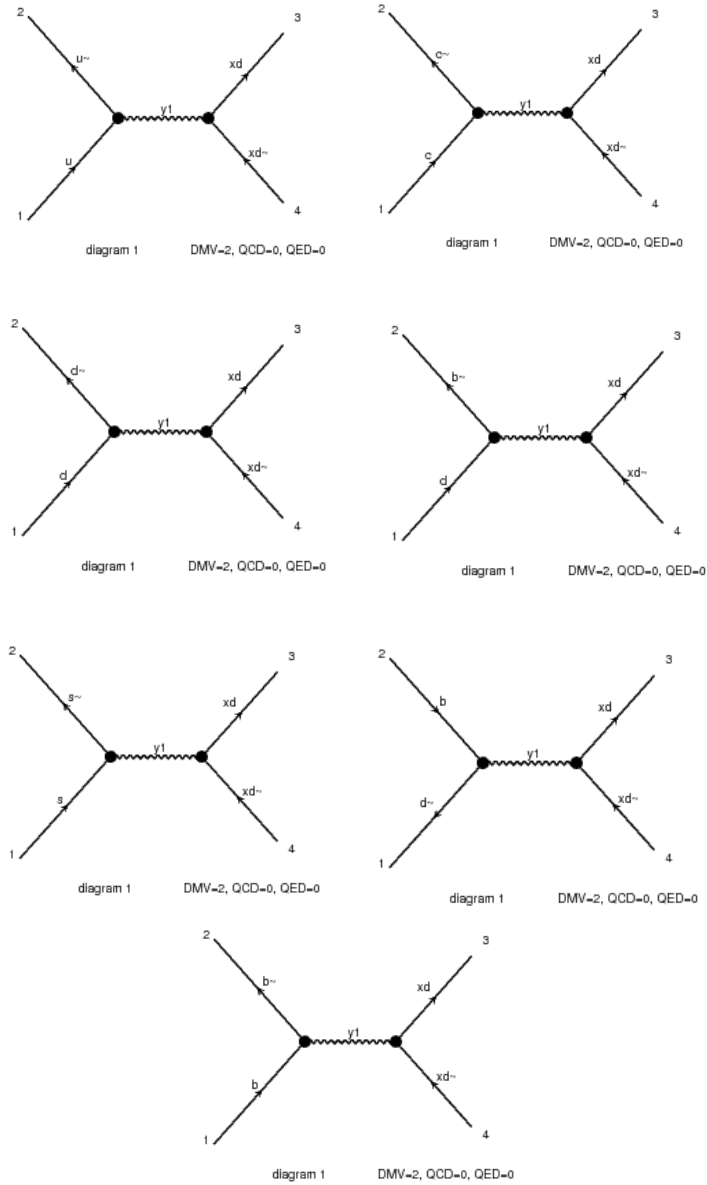


Figure 4. Feynman diagrams of $p p \rightarrow \chi_d \widetilde{\chi}_d$ with spin 1.

(2) $p p \rightarrow \chi_a \widetilde{\chi}_a \gamma$ (spin 0) total 20 diagrams (4 independent)

Figure 5 shows the Feynman diagrams of $p p \rightarrow \chi_a \widetilde{\chi}_a \gamma$ with spin 0. It shows the 4 independent Feynman diagrams.

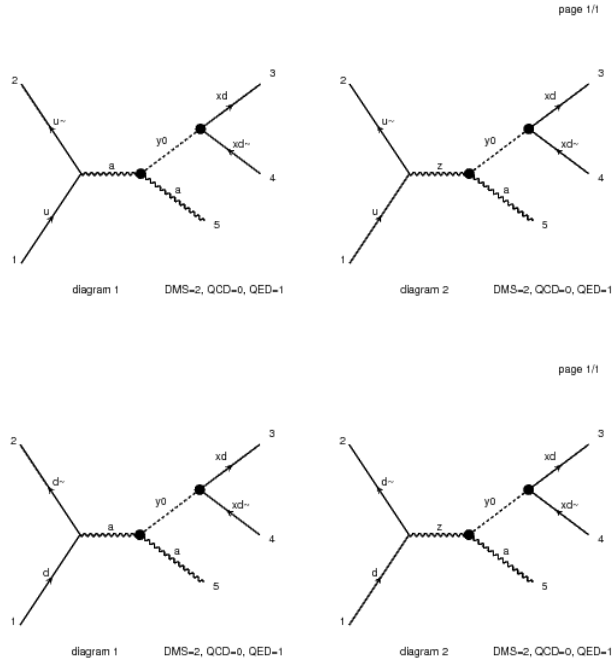


Figure 5. Feynman diagrams of $p p \rightarrow \chi_a \widetilde{\chi}_a \gamma$ with spin 0.

(3) $pp \rightarrow \chi_d \widetilde{\chi}_d \gamma$ (spin 1) total 28 diagrams (14 independent)

Figure 6 shows the Feynman diagrams of $pp \rightarrow \chi_d \widetilde{\chi}_d \gamma$ with spin 1. It shows the 14 independent Feynman diagrams.

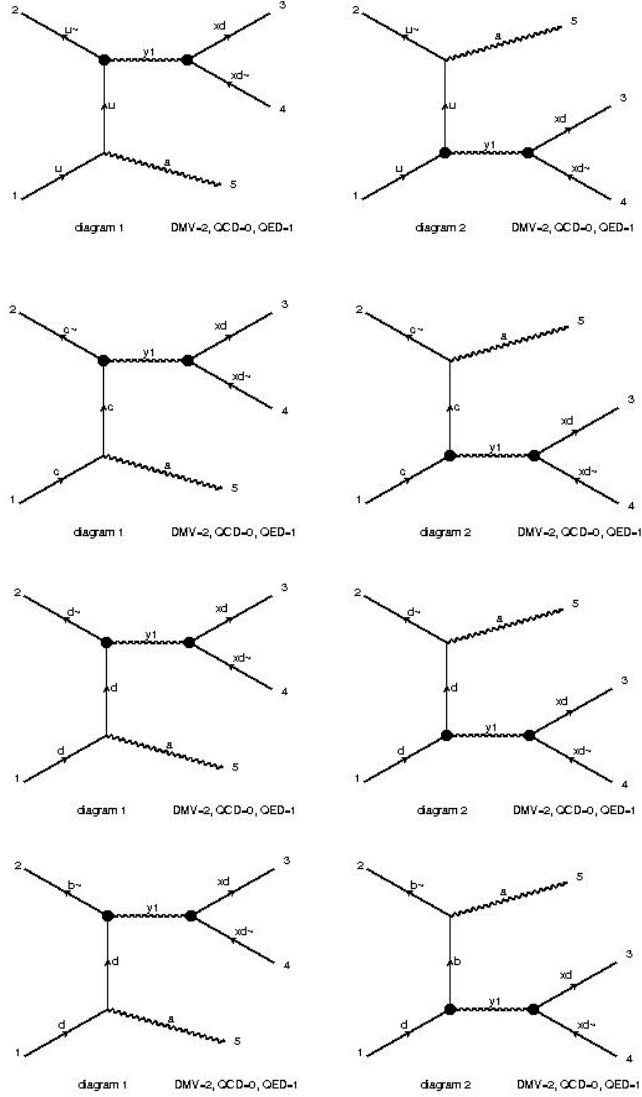


Figure 6. Feynman diagrams of $pp \rightarrow \chi_d \widetilde{\chi}_d \gamma$ with spin 1.

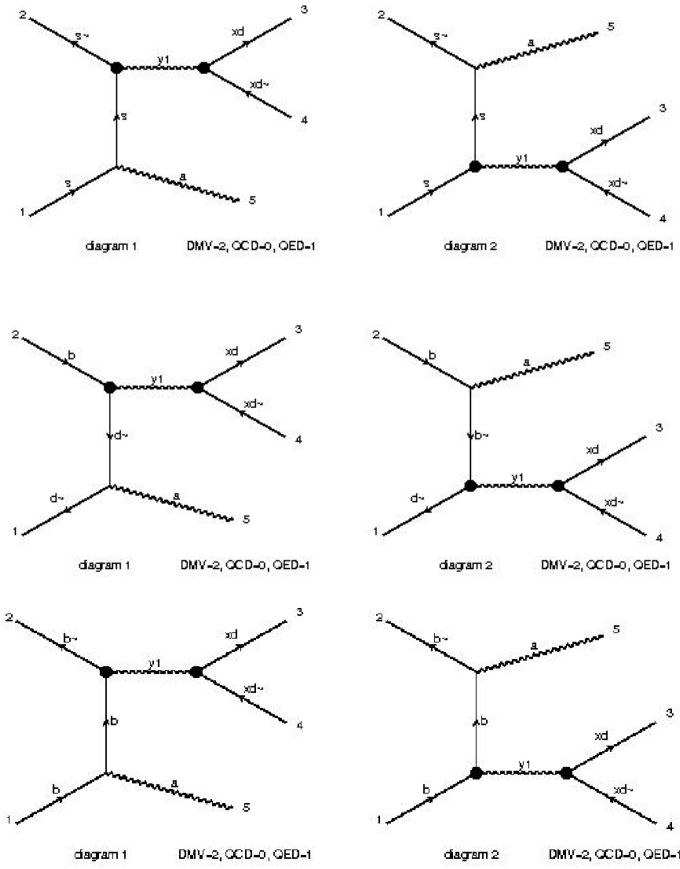


Figure 6. Feynman diagrams of $p p \rightarrow \chi_a \tilde{\chi}_a \gamma$ with spin 1 (continued).

(4) $e^+e^- \rightarrow \chi_d \widetilde{\chi}_d \gamma$ (spin 0) total 2 diagrams (2 independent)

Figure 7 shows the Feynman diagrams of $e^+e^- \rightarrow \chi_d \widetilde{\chi}_d \gamma$ with spin 0. It shows the 2 independent Feynman diagrams.

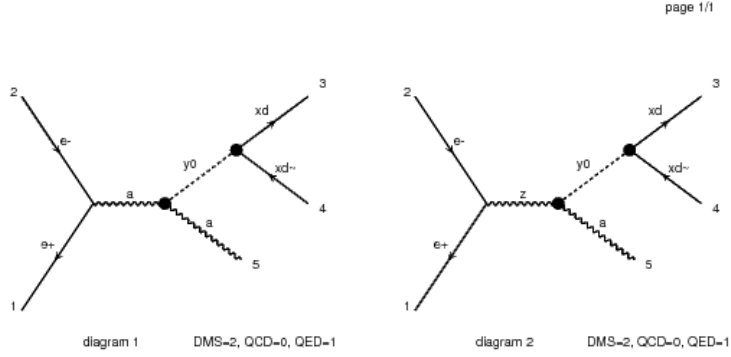


Figure 7. Feynman diagrams of $e^+e^- \rightarrow \chi_d \widetilde{\chi}_d \gamma$ with spin 0.

There are three parameters related to the signal process. Those parameters are CM energy, mass of dark photon, and coupling constant. We have studied the dependence of parameters by plotting cross-section graphs. The energy range was chosen in consideration of present and/or future electron-positron collider experiments: Belle II (10.58 GeV), Future Circular Collider (FCC)-ee (91 GeV), FCC-ee (160 GeV), Circular Electron-Positron Collider (CEPC) (160 GeV), CEPC (240 GeV), and International Linear Collider (ILC) (500 GeV). The mass of dark photon ranges from 1 MeV to 250 GeV. As shown in Figure 8, four coupling constants, denoted as A, B, C, D, exist in the signal process. The coupling constants are specified in Table 2. A and B correspond to

electromagnetic coupling mediated by photon while C and D correspond to muon and dark photon coupling, respectively. We changed the coupling of muon and dark photon. Table 3 shows parameters of the present and/or future electron-positron colliders (Zyla P. A., et al 2020). Belle II is the ongoing experiment while FCC-ee, CEPC, and ILC are the future experiment.

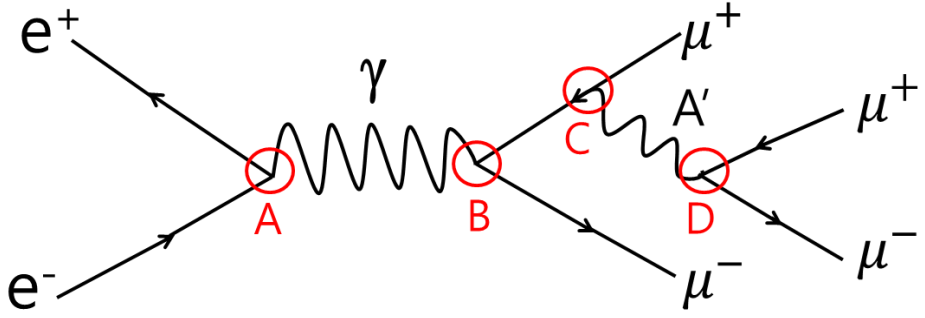


Figure 8. Feynman diagram illustrating the coupling constants.

Table 2. Identification of the coupling constants.

	Theory	MadGraph5	Default value	Description
A	α_{EW}^{-1}	aEWM1	1.325070×10^2	The inverse of the electromagnetic coupling
B	α_{EW}^{-1}	aEWM1	1.325070×10^2	The inverse of the electromagnetic coupling
C	$g_{l_{22}}^v$	gv122	1	Muon-Y1 vector (dark photon) coupling
D	$g_{l_{22}}^v$	gv122	1	Muon-Y1 vector (dark photon) coupling

Table 3. Parameters of the present and/or future electron-positron colliders ((Zyla P. A., et al 2020)).

	Belle II	FCC-ee	CEPC	ILC
Specification		Future Circular Collider	Circular Electron-Positron Collider	International Linear Collider
Site	Japan	France and Switzerland border	Chinese	Japan
Year	2018 -	2040 -	2030 -	-
Species	e^+e^-			
Type	circular	circular	circular	ILC
Beam energy (GeV)	$e^-: 7, e^+: 4$	46, 120, 183	46, 120	125, 250
Circumference / Length (km)	3.016	97.75	100	20.5, 31
Interaction regions	1	2	2	1
Peak luminosity ($10^{34} \text{ cm}^{-2} \text{ s}^{-1}$)	1.88	230, 8.5, 1.6	32, 3	1.4, 1.8
Integrated luminosity per experiment ($\text{ab}^{-1}/\text{year}$)	-	26, 0.9, 0.17	4, 0.4	0.2, 0.2
Delivered integrated luminosity per exp. (fb^{-1})	10.57	-	-	-

3. Methods

This section describes the series of processes performed in this study and the machines used. This study was conducted with a stand-alone frame and the Belle II Analysis Software Framework (basf2). Table 4 shows parameters of the stand-alone frame and the basf2. We scanned energy from 1 GeV to 500 GeV with the stand-alone frame. While, we only choose the 10.58 GeV for Belle II CM energy with the basf2. Figure 9 shows the flowcharts of the stand-alone frame and the basf2. First, we generated the electron-positron collider event using MadGraph5 (Alwall, J., et al., 2014) from the simplified model (Alves, D., et al., 2012), and the event simulation was performed on the Pythia8 framework (Sjöstrand T., et al., 2015). Next, the detector simulation was performed using Delphes (Favereau, J. D., et al., 2014). Finally, reconstruction was performed using MadAnalysis5 (Conte, Fuks B., & Serret G. 2013). The resulting file was generated in the root format for plotting (Antcheva, I., et al., 2009). Table 5 shows the software, code file, input file, and output file used at each step based on the stand-alone frame. The output file of the physics generation using the Madgraph5 is the `unweighed_events.lhe.gz` file. The `unweighed_events.lhe.gz` file is then used as an input file for detector simulation using MadAnalysis5 (Delphes) and reconstruction using MadAnalysis5 and the output files are root file and histogram macro file, respectively. Table 6 shows the software, code file, input file, and output file used at each step based on the basf2. The order of processing is physics generation, detector simulation, reconstruction, and fitting. At the physics generation, we have used the basf2 (MadGraph). At the detector

simulation, we have used the basf2 (Geant4). At the reconstruction, we have used the basf2. At the fitting, we have used ROOT. File directory is located in KEKCC work server.

Table 4. Parameters of the stand-alone frame and the basf2.

Software	Stand-alone frame	basf2
Energy	1 – 500 GeV	10.58 GeV
Detector	Delphes	Genat4
Computing resource	Local Linux machine	KEKCC work server
OS	Scientific Linux 6.5	CentOS Linux 7
Processor	Intel Xeon	Intel Xeon
	CPU X5560	Gold 6230
Architecture	2.8 GHz	2.1 GHz
	Multicore	Multicore

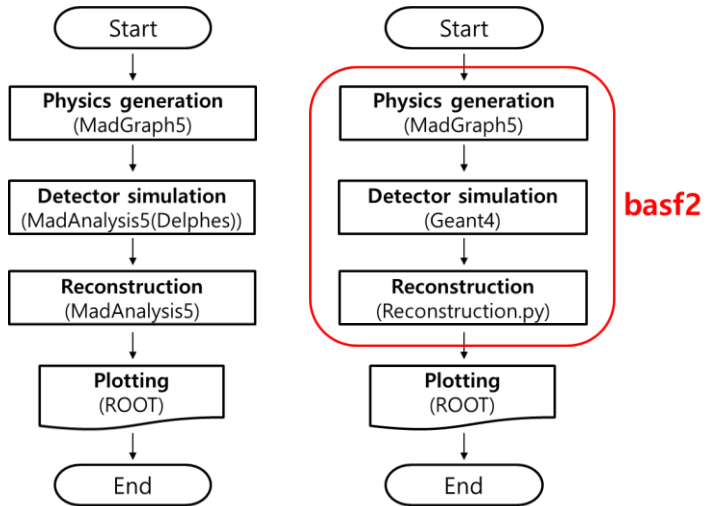


Figure 9. The flowcharts of the stand-alone frame (left) and the basf2 (right).

Table 5. Software, input file, and output file of processing based on the stand-alone frame.

Processing	Software	Input file	Output file
I. Physics generation	MadGraph5	model: simplified model	unweighed_events.lhe.gz
II. Detector simulation	MadAnalysis5 (Delphes)	unweighed_events.lhe.gz	cms_edited_0.3_new.root
III. Reconstruction	MadAnalysis5	unweighed_events.lhe.gz (Parton level)	selection_1.C (histogram macros, etc)
IV. Fitting	ROOT		

Table 6. Software, code file, input file, and output file of processing based on the basf2.

Processing	Software	Code file	Input file	Output file
I. Physics generation	basf2 (MadGraph5)	generation_zprimetomu mu.py	model: Zprime_Lmu_Ltau	unweighed_events.lhe.gz
	basf2 (.lhe ->.root)	generation_zprimetomu mu.py	unweighed_events.lhe.gz -> unweighed_events.lhe	zprimetomumu_0.3_lhe.root [LHE format]
II. Simulation	basf2 (Geant4)	SimulateAndReconstruct _zprimetomumu.py	zprimetomumu_0.3_lhe.root [LHE format]	simulation_and_reconstruction_mdst .root [MDST format]
III. Reconstruction	basf2	reconstruct_zprimetomu mu.py	simulation_and_reconstructi on_ mdst.root [MDST format]	zprimetomumu_ntuple.root [Ntuple format]
IV. Fitting	ROOT			

Table7 shows the specification of the machine used in the stand-alone frame and the basf2. The local Linux machine was used in the stand-alone frame study and the KEKCC work server was used in the basf2 study. Details are as shown in the table 7.

Table 7. The specification of the machine used in the stand-alone frame and the basf2.

	Stand-alone frame	basf2
Machine	Local Linux machine	KEKCC work server
OS	Scientific Linux 6.5	CentOS Linux 7
Processor	Intel Xeon CPU X5560 2.8 GHz	Intel Xeon Gold 6230 2.1 GHz
Architecture	Multicore	Multicore
Number of cores/CPU	4	20
Number of CPUs/node	8	40
Number of cores/node	32	800
Number of total nodes	1	2
Number of total cores	32	1600

4. Results

4.1 Background study using the standard model

We have used the SM as a background events. The process is $e^+e^- \rightarrow \mu^+\mu^-\mu^+\mu^-$. There are total 48 Feynman diagrams of background process. Table 8 shows the settings for the SM event generation. The local Linux machine was used. The events were generated using MadGraph5 v2.6.4 (Alwall, J., et al., 2014) with the default parameter card, Pythia8 (Sjöstrand T., et al., 2015), default Delphes (Favereau, J. D., et al., 2014), and MadAnalysis5 (Conte, Fuks B., & Serret G. 2013). We have generated four muon final states for the SM. The number of events was 10,000. The range of CM energy is from 50 GeV to 500 GeV by 10 GeV. This range of CM energy includes the FCC-ee (91 GeV), FCC-ee (160 GeV), CEPC (160 GeV), CEPC (240 GeV) and ILC (500 GeV) as representative e^+e^- colliders in present and/or future. Events with CM energy of less than 40 GeV were not generated because of the zero cross-section.

Table 8. The settings for the standard model (SM) event generation.

Specification	Content
Machine	Local Linux machine
Simulation tool kit	MadGraph5 v2.6.4
Software	Pythia8, Delphes (CMS), MadAnalysis5
Imported model	Standard model (default)
Command for process	generate e+ e- > mu+ mu- mu+ mu-
Number of events	10,000
CM energy	50, 60, ..., 490, 500 GeV

The mediator particles in all the Feynman diagrams were photons or Z bosons. Figure 10 shows the cross-section of the SM event depending on CM energies (Park, K., & Cho, K., 2021). A total of 48 modes are involved in the process.

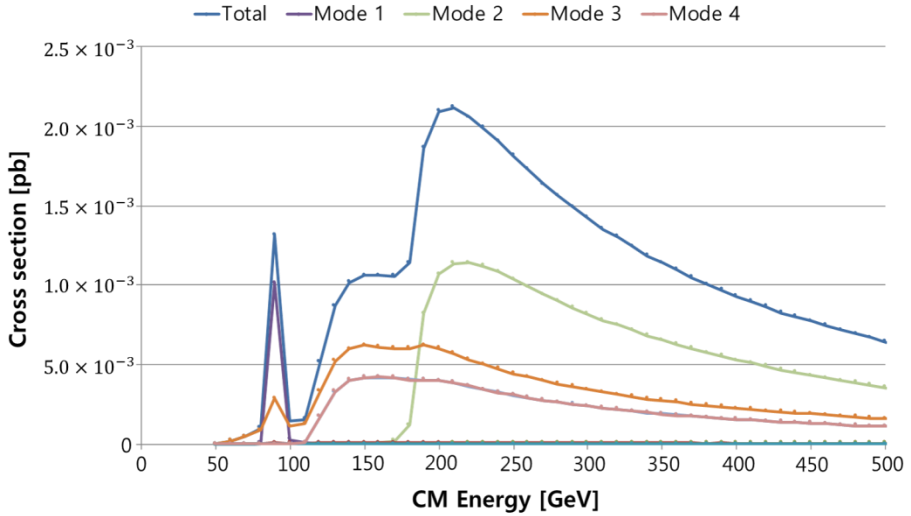


Figure 10. Standard model (SM) cross-section for different center of mass (CM) energies.

Figure 11 shows the dominant modes of the SM. Mode 1 contributed to the first peak at approximately 90 GeV, attributable to the Z boson interaction. The second peak, which occurred near 210 GeV, corresponded to the maximum cross-section. This peak could be attributed to the presence of two Z bosons as mediator particles.

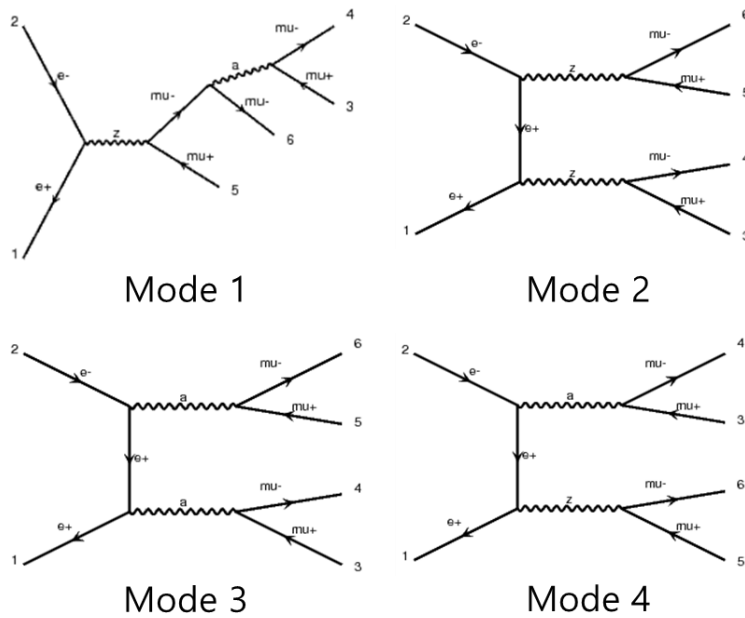
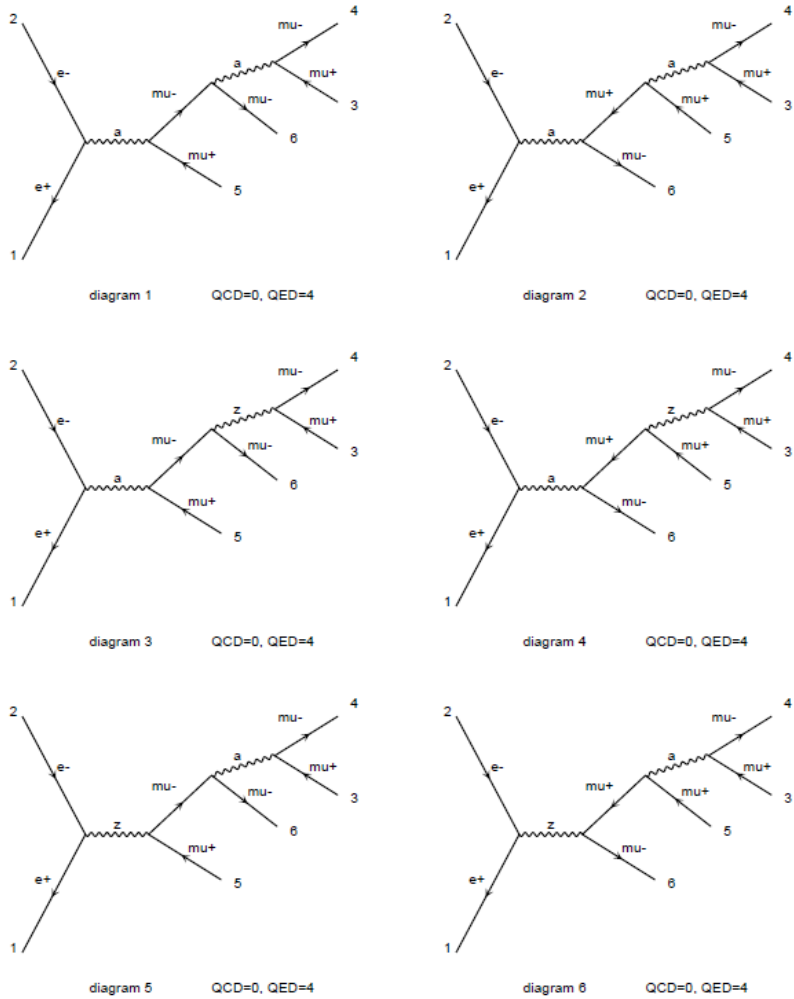


Figure 11. The Feynman diagrams of dominant modes of the standard model.

Figure 12 shows that total 48 Feynman diagrams of background.

page 1/7



Diagrams made by MadGraph5_aMC@NLO

Figure 12. Total 48 Feynman diagrams of background process.

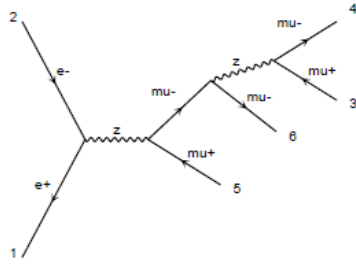


diagram 7 QCD=0, QED=4

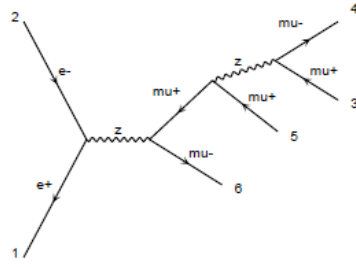


diagram 8 QCD=0, QED=4

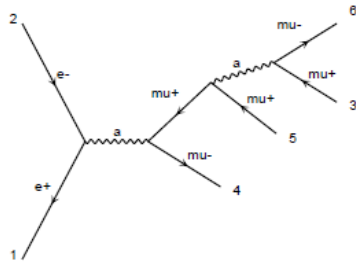


diagram 9 QCD=0, QED=4

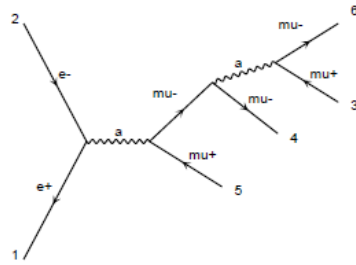


diagram 10 QCD=0, QED=4

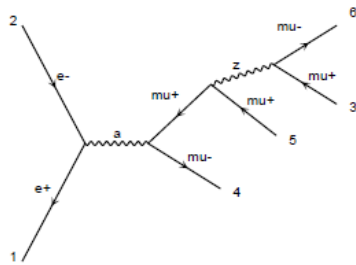


diagram 11 QCD=0, QED=4

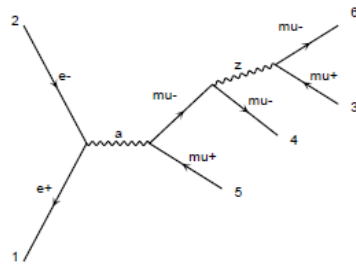


diagram 12 QCD=0, QED=4

Diagrams made by MadGraph5_aMC@NLO

Figure 12. Total 48 Feynman diagrams of background process (continued).

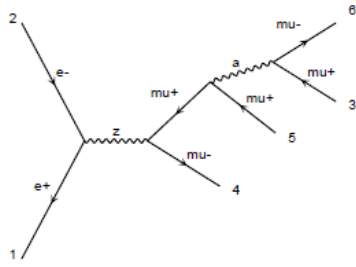


diagram 13 QCD=0, QED=4

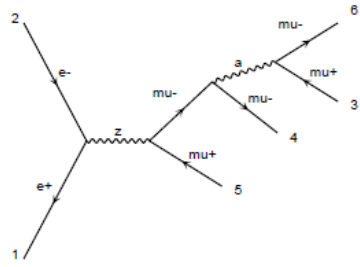


diagram 14 QCD=0, QED=4

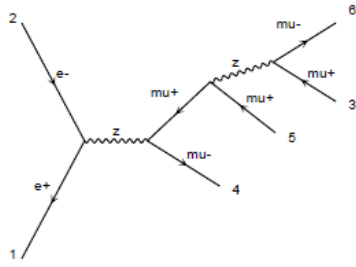


diagram 15 QCD=0, QED=4

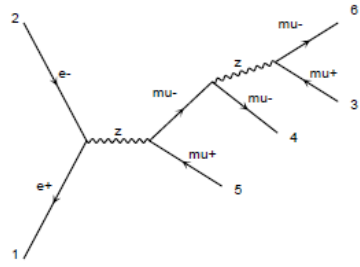


diagram 16 QCD=0, QED=4

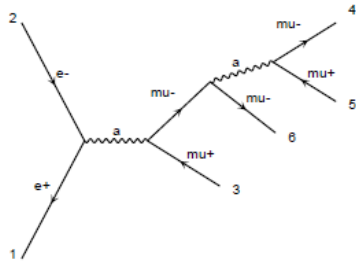


diagram 17 QCD=0, QED=4

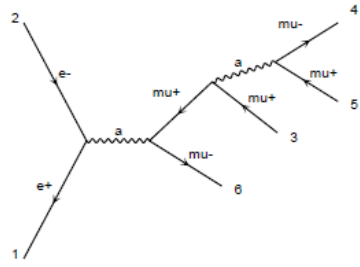


diagram 18 QCD=0, QED=4

Diagrams made by MadGraph5_aMC@NLO

Figure 12. Total 48 Feynman diagrams of background process (continued).

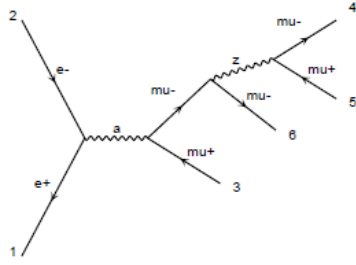


diagram 19 QCD=0, QED=4

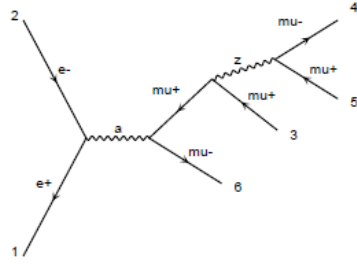


diagram 20 QCD=0, QED=4

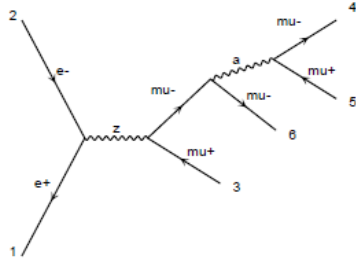


diagram 21 QCD=0, QED=4

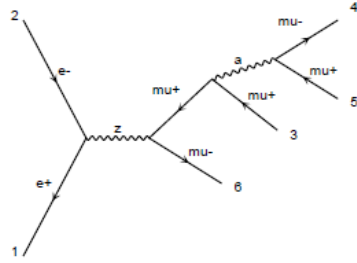


diagram 22 QCD=0, QED=4

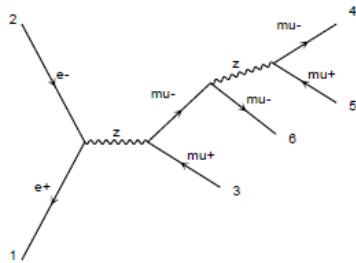


diagram 23 QCD=0, QED=4

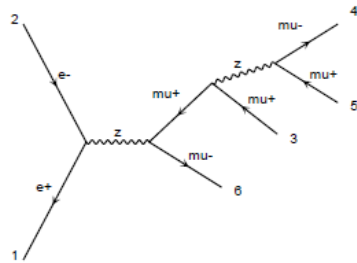


diagram 24 QCD=0, QED=4

Diagrams made by MadGraph5_aMC@NLO

Figure 12. Total 48 Feynman diagrams of background process (continued).

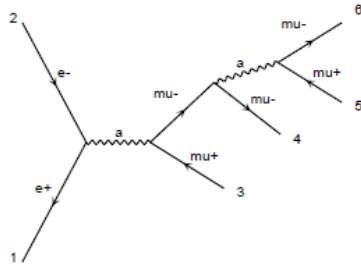


diagram 25 QCD=0, QED=4

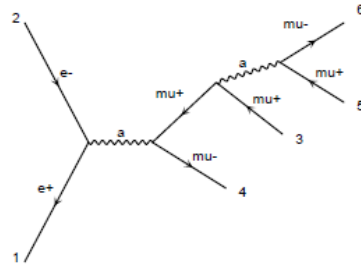


diagram 26 QCD=0, QED=4

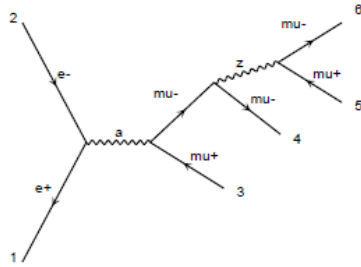


diagram 27 QCD=0, QED=4

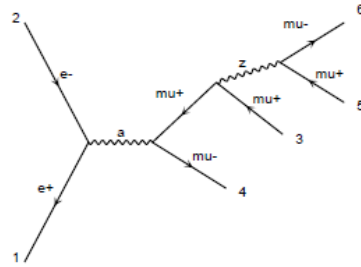


diagram 28 QCD=0, QED=4

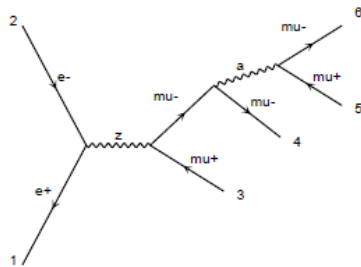


diagram 29 QCD=0, QED=4

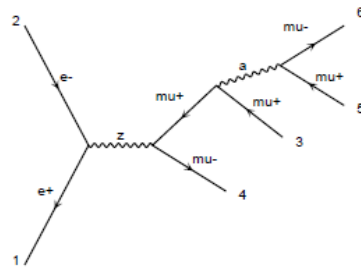


diagram 30 QCD=0, QED=4

Diagrams made by MadGraph5_aMC@NLO

Figure 12. Total 48 Feynman diagrams of background process (continued).

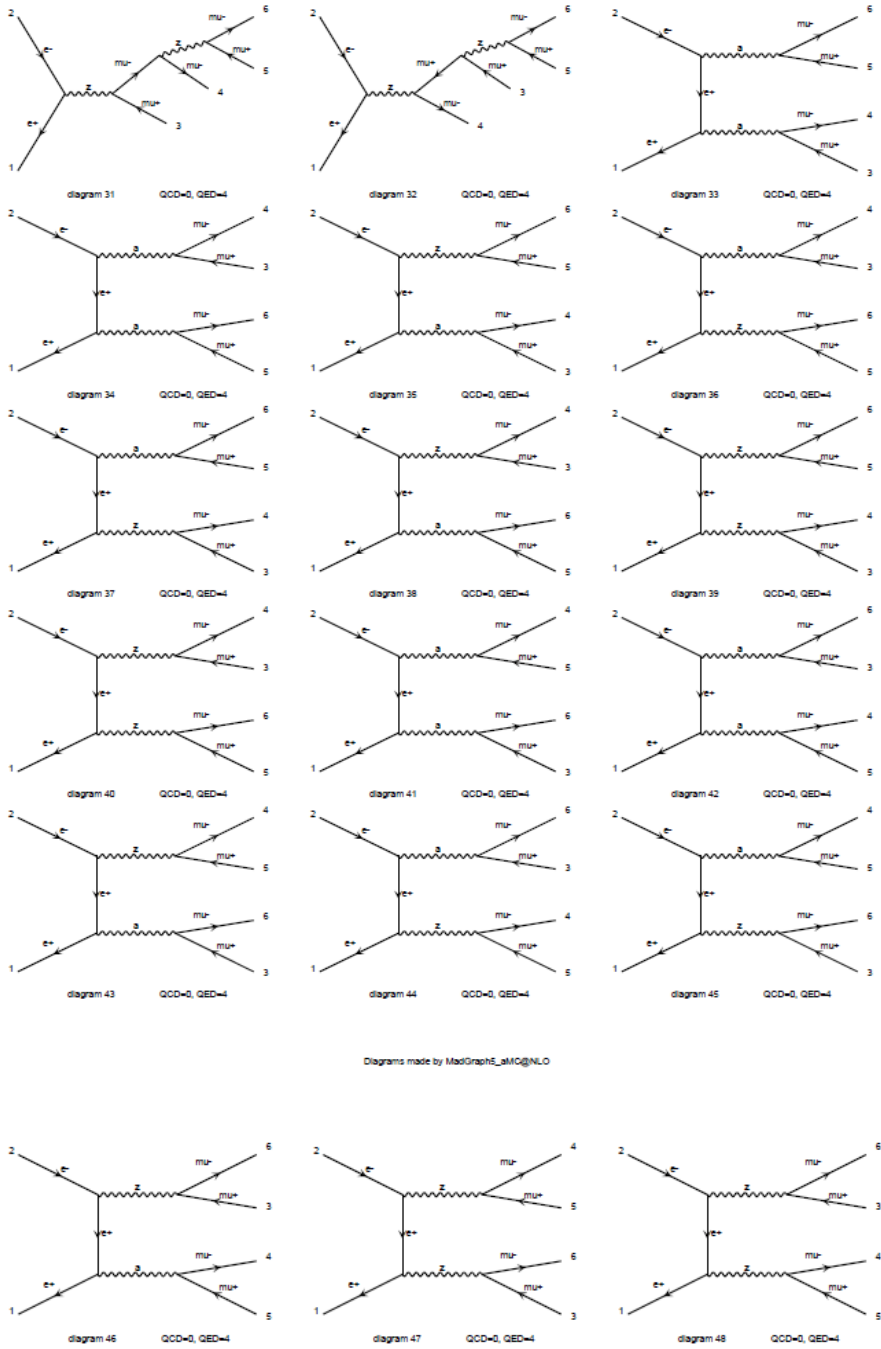


Figure 12. Total 48 Feynman diagrams of background process (continued).

4.2 Signal channel studies based on the stand-alone frame

4.2.1 Studies at generation level

The signal process is $e^+ e^- \rightarrow \mu^+ \mu^- A'$ with $A' \rightarrow \mu^+ \mu^-$. When the CM energy was less than 30 GeV, the process of the photon interaction was applied, as these interactions are dominant in this CM energy range. Because three parameters are involved in the generation of signal events, we examined the dependence of the cross-section on each parameter sequentially. The signal events were generated using the settings listed in Table 9 (Park, K., & Cho, K., 2021). Figure 13 shows the Feynman diagrams of the signal event (Park, K., & Cho, K., 2021). Two processes were considered: (a) $e^+ e^- \rightarrow \gamma \rightarrow \mu^+ \mu^- A'$ with $A' \rightarrow \mu^+ \mu^-$ and (b) $e^+ e^- \rightarrow \mu^+ \mu^- A'$ with $A' \rightarrow \mu^+ \mu^-$. Only process (a) had appeared when the CM energy was less than 30 GeV.

Table 9. The settings for the signal event generation.

Specification	Content
Machine	Local Linux machine
Simulation tool kit	MadGraph5 v2.6.4
Software	Pythia8, Delphes (CMS), MadAnalysis5
Imported model	DMsimp_s_spin1
Command for process (a)	$e^+ e^- \rightarrow a, (a \rightarrow \mu^+ \mu^- \gamma, \gamma \rightarrow \mu^+ \mu^-)$
Command for process (b)	$e^+ e^- \rightarrow \mu^+ \mu^- \gamma, \gamma \rightarrow \mu^+ \mu^-$
Number of events	10,000

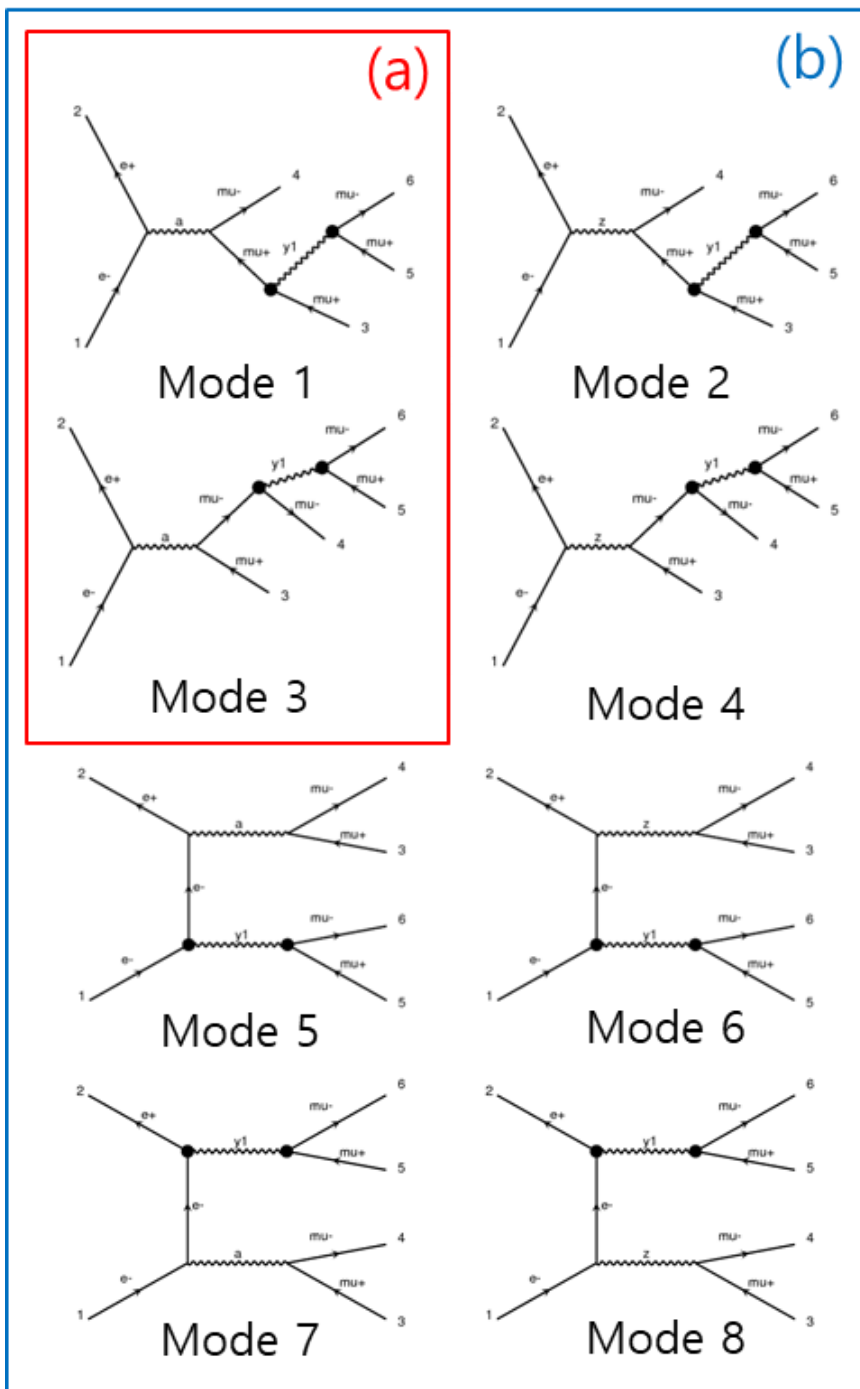


Figure 13. The possible Feynman diagrams of the signal mode.

Table 10 shows the primary/secondary mediator of the signal process. Mode 2, which have Z boson as a primary mediator, contributes to the peak at 90 GeV.

Table 10. Primary/secondary mediator of the signal process.

	Primary mediator	Secondary mediator
Mode 1	γ	A'
Mode 2	Z boson	A'
Mode 3	γ	A'
Mode 4	Z boson	A'
Mode 5	γ, A'	–
Mode 6	Z boson, A'	–
Mode 7	γ, A'	–
Mode 8	Z boson, A'	–

[Cross-section dependence on the center of mass energy]

Figure 14 shows the cross-section dependence on the center of mass (CM) energy. The CM energy increased from 10 GeV to 500 GeV by 10 GeV steps. The mass of dark photon was fixed at 0.3 GeV with the width, 6.7×10^{-6} GeV. The coupling constant was 0.1. At energies less than 30 GeV, process (a) was implemented. As shown in Figure 14, the cross-section was maximized at the Z boson mass of 90 GeV. In case that the CM energy is greater than 90 GeV, the cross-section decreases as CM energy increases. The part marked in red shows the process (a) and the part marked in yellow shows the process (b).

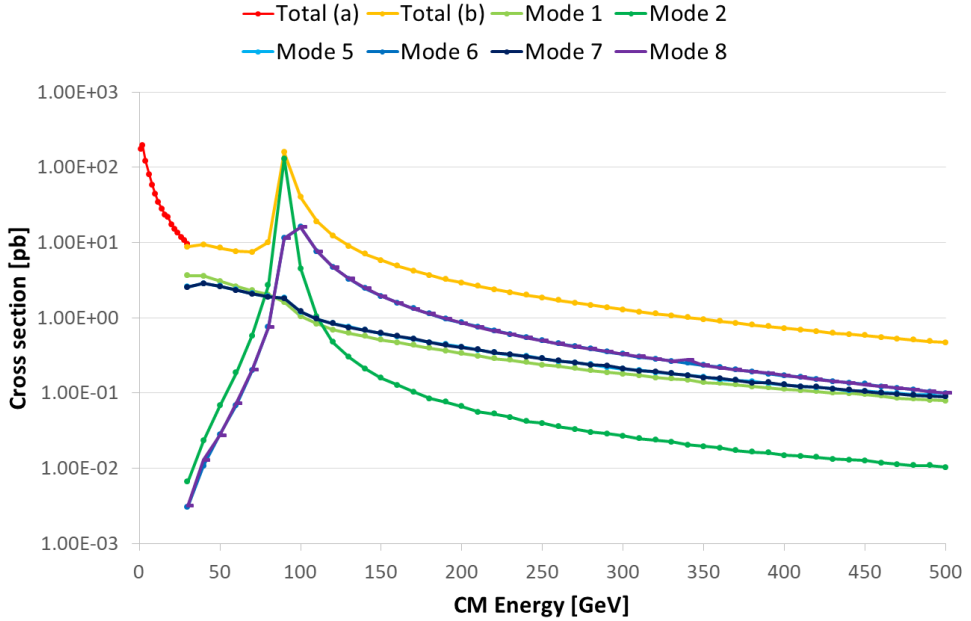


Figure 14. Cross-section dependence on the center of mass (CM) energy.

[Cross-section dependence on the mass of dark photon]

Figure 15 shows the cross-section dependence on the mass of dark photon. The coupling constant was set as 0.1. The mass of dark photon was varied from 1 MeV to 250 GeV and the CM energy was fixed at 10.58 GeV, 91 GeV, 160 GeV, 240 GeV, and 500 GeV with the width, 6.7×10^{-6} GeV.

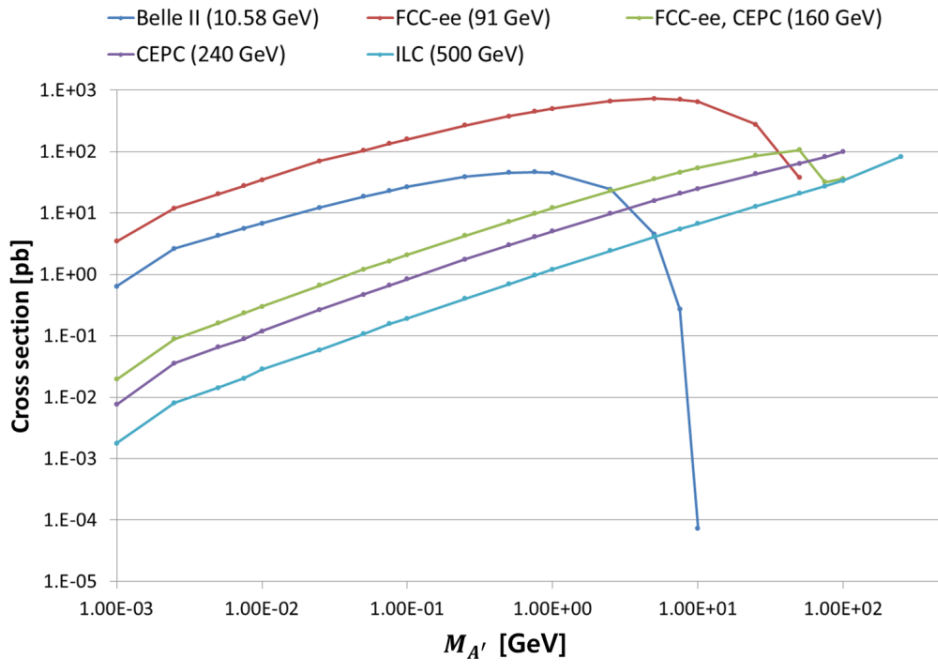


Figure 15. Cross-section dependence on the mass of dark photon.

[Cross-section dependence on the coupling constant]

Figure 16 shows the cross-section dependence on the coupling constant. The coupling constant of the muon and dark photon ($g_{\nu 22}$) was varied and the coupling constant of the SM (a_{EWM1}) was used as the default value. We changed the coupling constant from 0.01 to 1. The cross-section increased as the coupling constant increased.

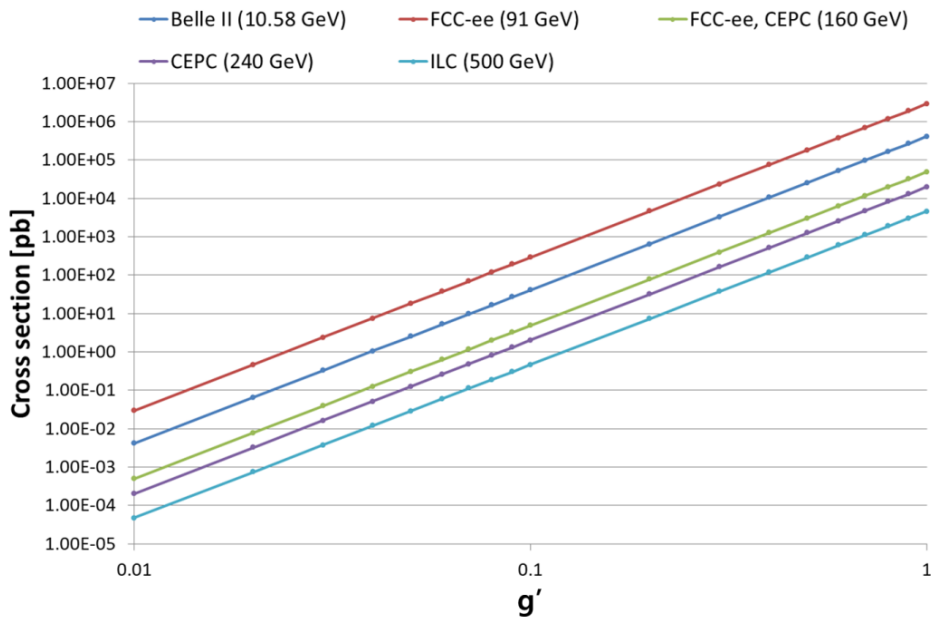


Figure 16. Cross-section dependence on the coupling constant.

[Cross-section dependence on the CM energy varying the mass of dark photon]

Figure 17 shows the cross-section dependence on the CM energy varying the mass of dark photon. The used CM energy varied from 10 GeV to 500 GeV by 10 GeV. The used masses of dark photon are 0.001, 0.0025, ..., 50, 75, 100 GeV with the width, 6.7×10^{-6} GeV. The coupling constant (g_{V11} , g_{V22}) was fixed to 1.

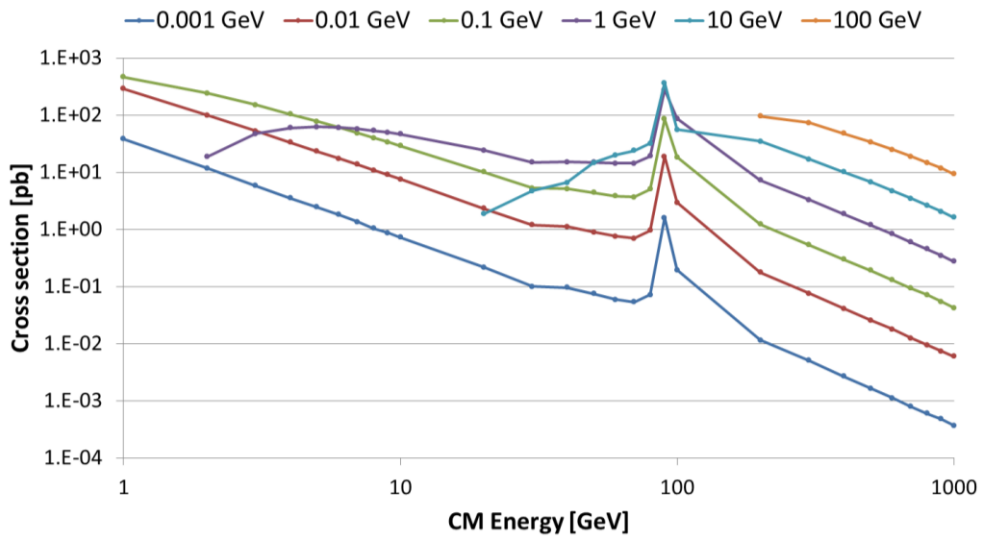


Figure 17. Cross-section dependence on the CM energy varying the mass of dark photon.

4.2.2 Studies at reconstruction level

At the reconstruction level, we have used energies of Belle II (10.58 GeV), FCC-ee (91 GeV), FCC-ee (160 GeV), CEPC (160 GeV), CEPC (240 GeV), and ILC (500 GeV). Table 11 shows settings for reconstruction level study. The mass of dark photon was 0.3 GeV with the width, 6.7×10^{-6} GeV. The coupling constant was 0.1. The number of events was 10,000. Table 12 shows the CM energy, signal process, η cut, and Delphes cards on electron-positron collider experiments. Delphes cards can be downloaded from the following website:

<https://cp3.irmp.ucl.ac.be/projects/delphes/browser/git/cards>.

Table 11. The settings for reconstruction level study.

Specification	Content
Machine	Local Linux machine
Imported model	DMsimp_s_spin1
Command for process	$e^+ e^- \rightarrow a, (a \rightarrow \mu^+ \mu^- \gamma_1, \gamma_1 \rightarrow \mu^+ \mu^-)$
Number of events	10,000
Mass of dark photon	0.3 GeV
(width)	$(6.7 \times 10^{-6} \text{ GeV})$
Coupling constant	0.1

Table 12. CM energy, signal process, η cut, Delphes card on e+ e- collider experiments.

Experiments	CM energy [GeV]	Signal process	η cut	Delphes card
Belle II	10.58 GeV	$e^+ e^- \rightarrow \gamma \rightarrow \mu^+ \mu^- A'$	$-1.317 \leq \eta \leq 1.901$	delphes_card_CMS.tcl
	(e^- : 7 GeV, e^+ : 4 GeV)	with $A' \rightarrow \mu^+ \mu^-$		(eta cut edit)
FCC-ee	91 GeV (e^\pm : 45.5 GeV)	$e^+ e^- \rightarrow \mu^+ \mu^- A'$	$-3.0 \leq \eta \leq 3.0$	delphes_card_IDEA.tcl
	160 GeV (e^\pm : 80 GeV)			
CEPC	160 GeV (e^\pm : 80 GeV)	with $A' \rightarrow \mu^+ \mu^-$	$-3.0 \leq \eta \leq 3.0$	delphes_card_CEPC.tcl
	240 GeV (e^\pm : 120 GeV)			
ILC	500 GeV (e^\pm : 250 GeV)		$-2.4 \leq \eta \leq 2.4$	delphes_card_ILD.tcl

[Belle II (10.58 GeV)]

Figure 18 shows the comparison of generation level and reconstruction level at the Belle II (10.58 GeV).

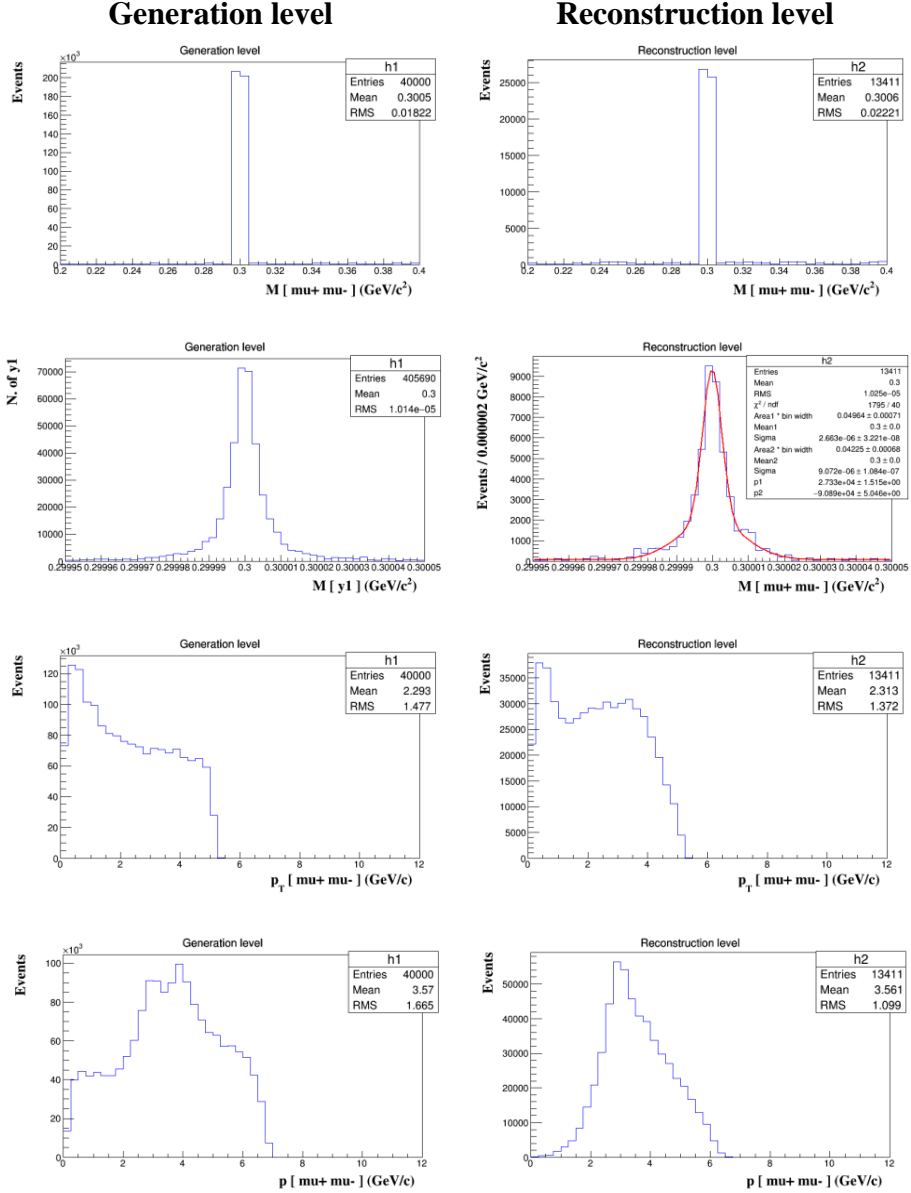


Figure 18. Comparison of generation level and reconstruction level at the Belle II (10.58 GeV). Number of events (y-axis) are multiplied by cross-section (40.6 pb).

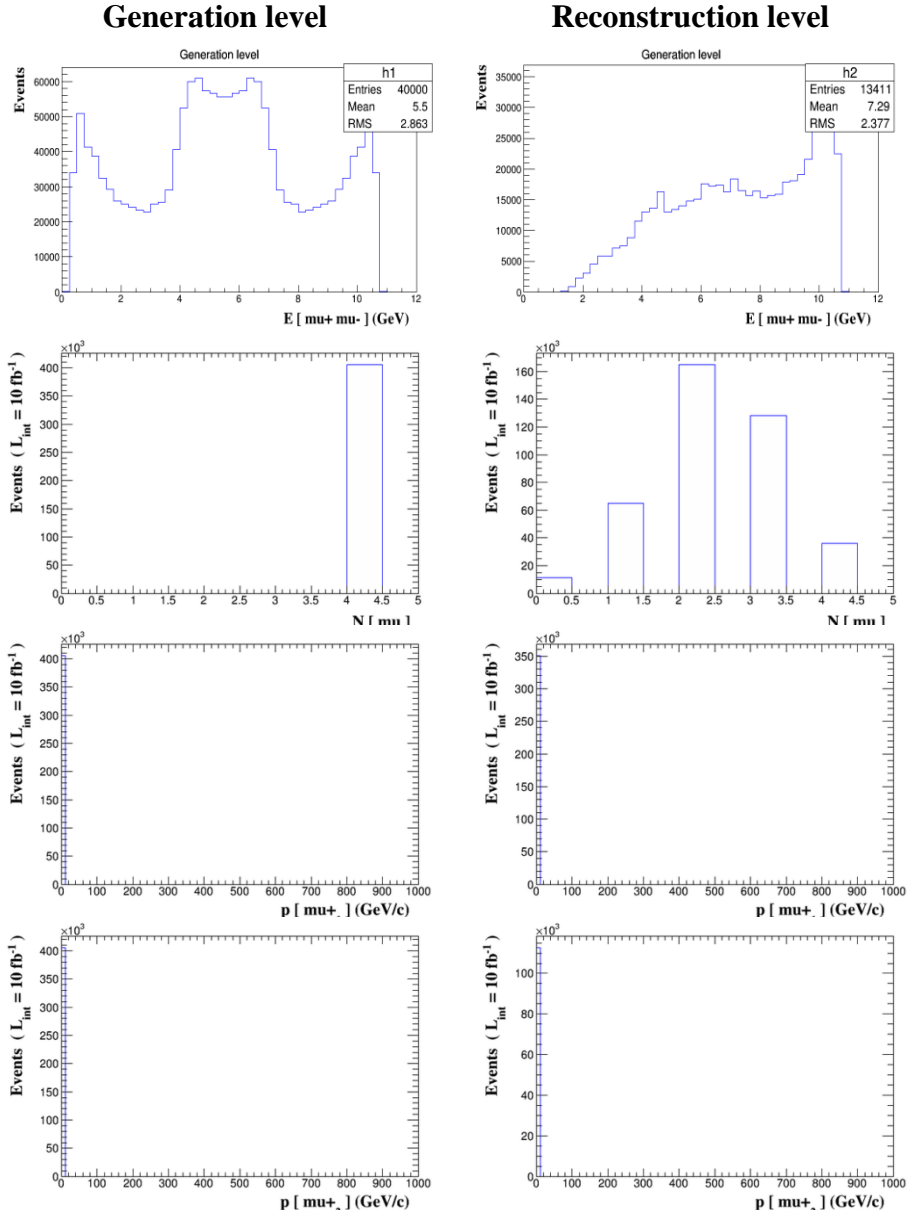


Figure 18. Comparison of generation level and reconstruction level at the Belle II (10.58 GeV). Number of events (y-axis) are multiplied by cross-section (40.6 pb) (continued).

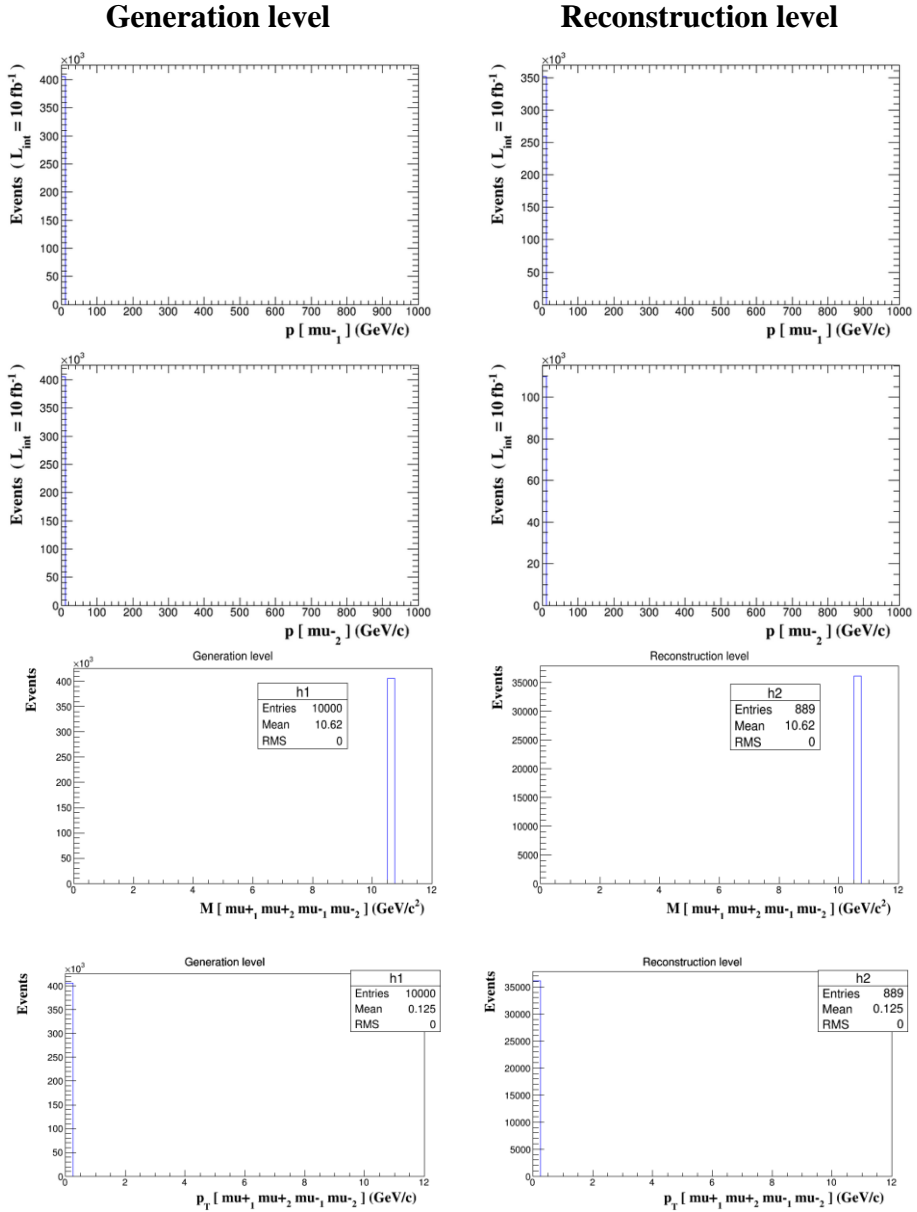


Figure 18. Comparison of generation level and reconstruction level at the Belle II (10.58 GeV). Number of events (y-axis) are multiplied by cross-section (40.6 pb) (continued).

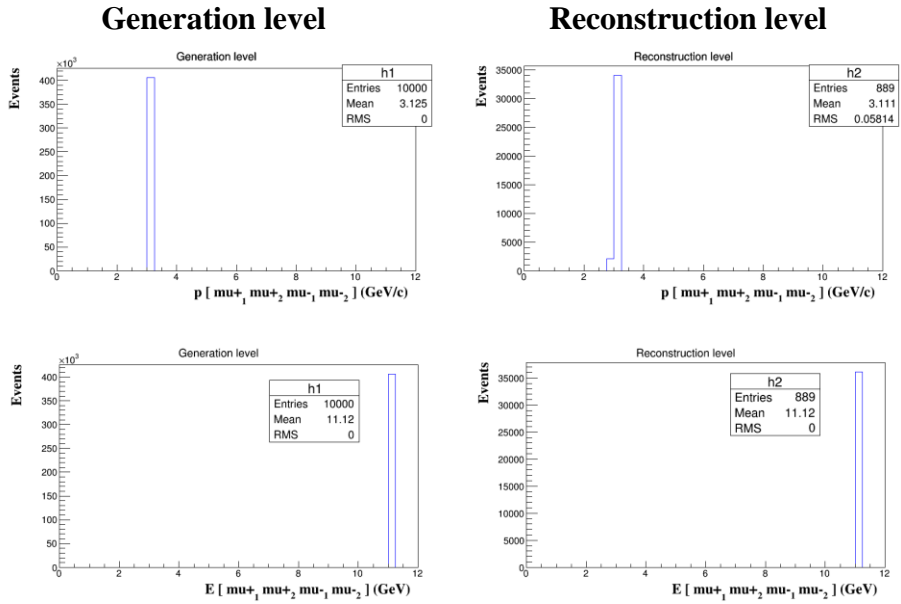


Figure 18. Comparison of generation level and reconstruction level at the Belle II (10.58 GeV). Number of events (y-axis) are multiplied by cross-section (40.6 pb) (continued).

[FCC-ee (91 GeV)]

Figure 19 shows the comparison of generation level and reconstruction level at the FCC-ee (91 GeV).

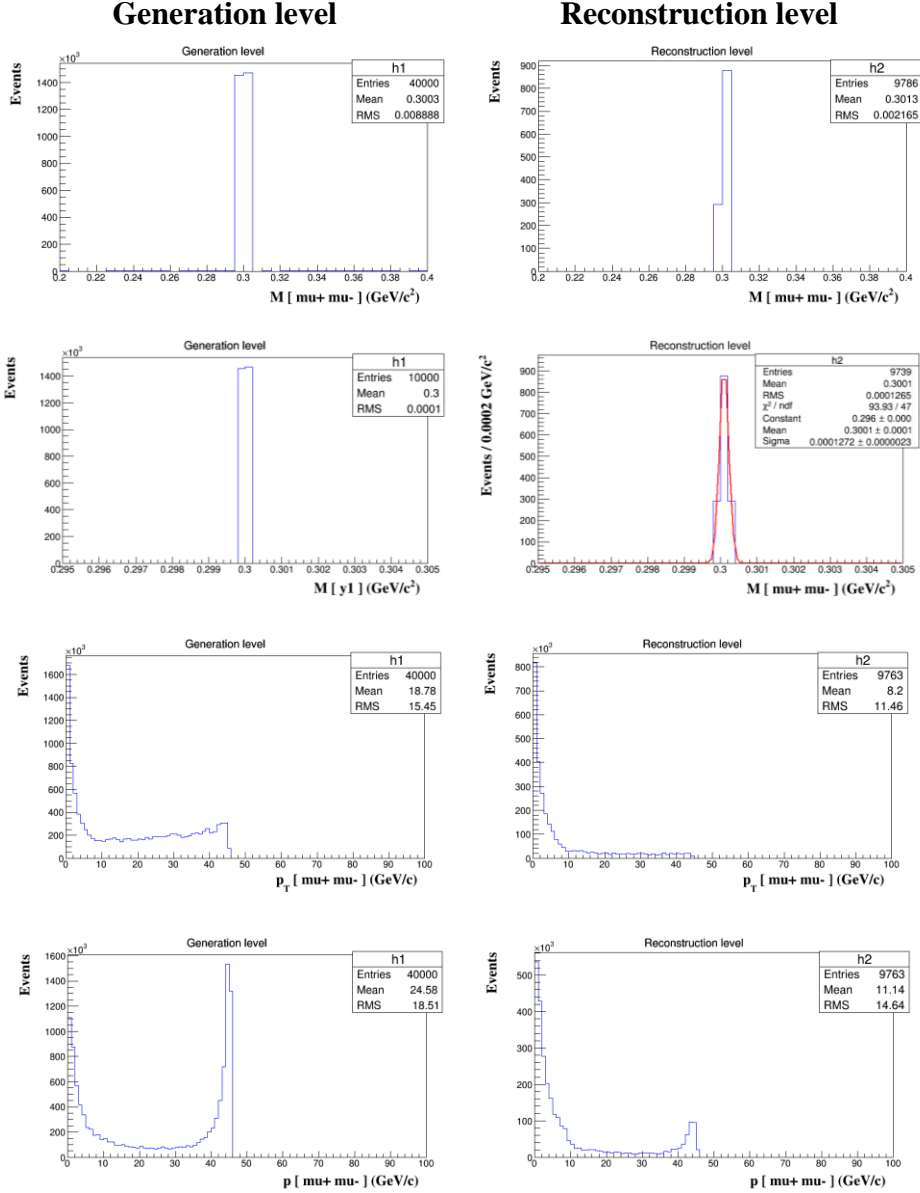


Figure 19. Comparison of generation level and reconstruction level at the FCC-ee (91 GeV). Number of events (y-axis) are multiplied by cross-section (292 pb).

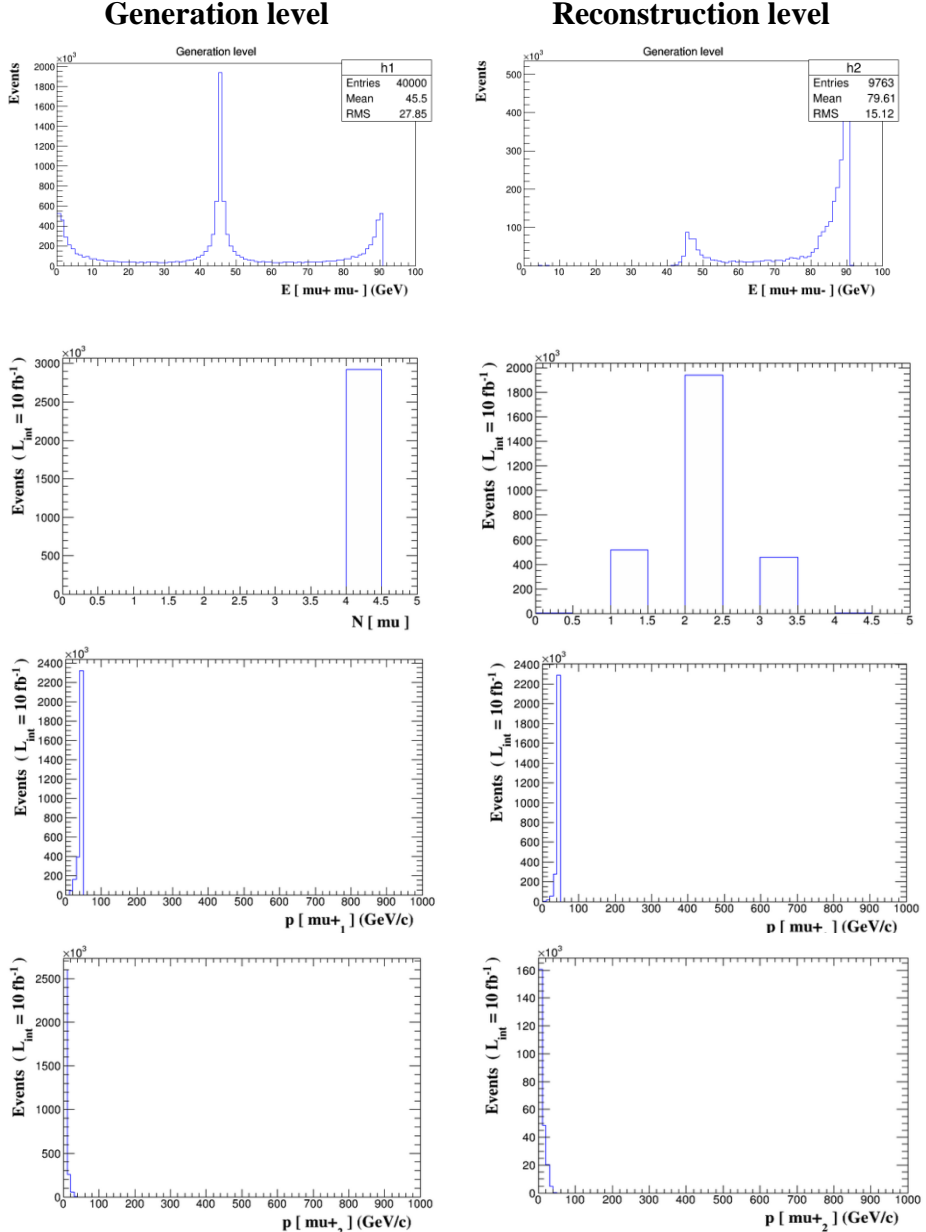


Figure 19. Comparison of generation level and reconstruction level at the FCC-ee (91 GeV). Number of events (y-axis) are multiplied by cross-section (292 pb) (continued).

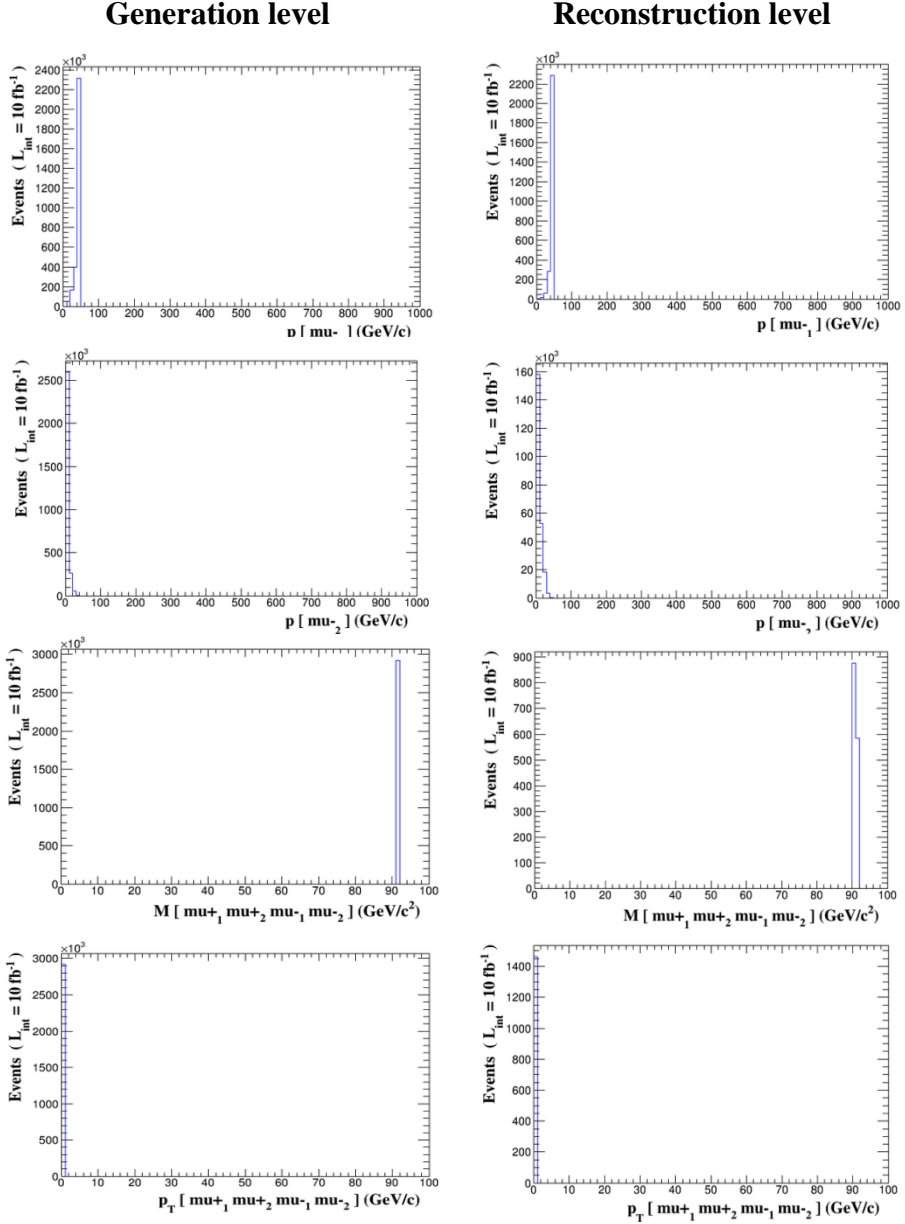


Figure 19. Comparison of generation level and reconstruction level at the FCC-ee (91 GeV). Number of events (y-axis) are multiplied by cross-section (292 pb) (continued).

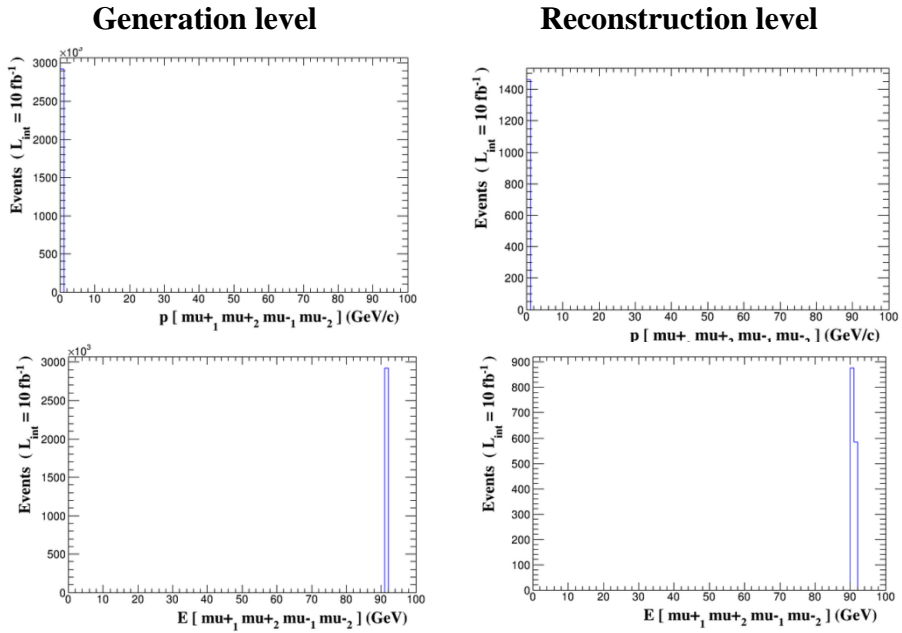


Figure 19. Comparison of generation level and reconstruction level at the FCC-ee (91 GeV). Number of events (y-axis) are multiplied by cross-section (292 pb) (continued).

[FCC-ee (160 GeV)]

Figure 20 shows the comparison of generation level and reconstruction level at the FCC-ee (160 GeV).

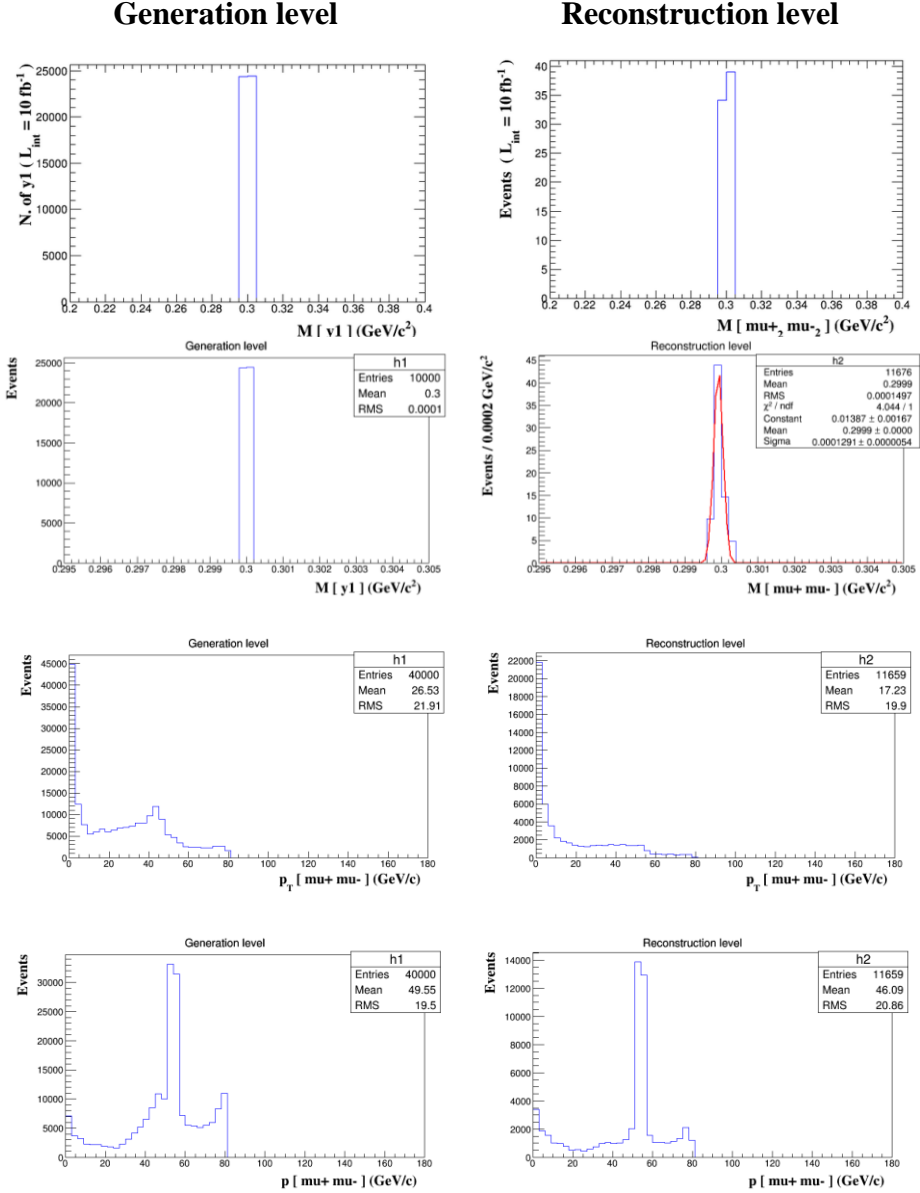


Figure 20. Comparison of generation level and reconstruction level at the FCC-ee (160 GeV). Number of events (y -axis) are multiplied by cross-section (4.88 pb).

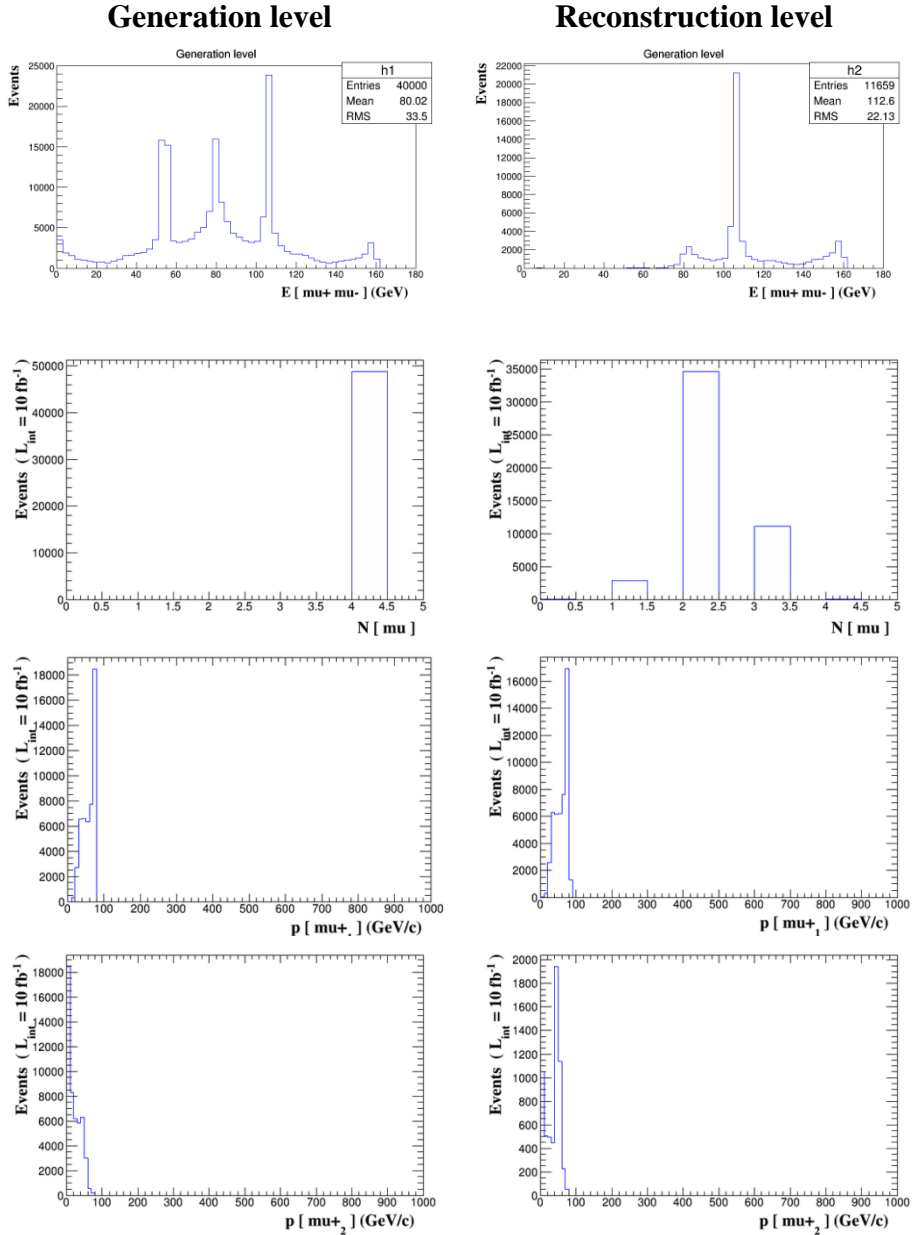


Figure 20. Comparison of generation level and reconstruction level at the FCC-ee (160 GeV). Number of events (y -axis) are multiplied by cross-section (4.88 pb) (continued).

Generation level

Reconstruction level

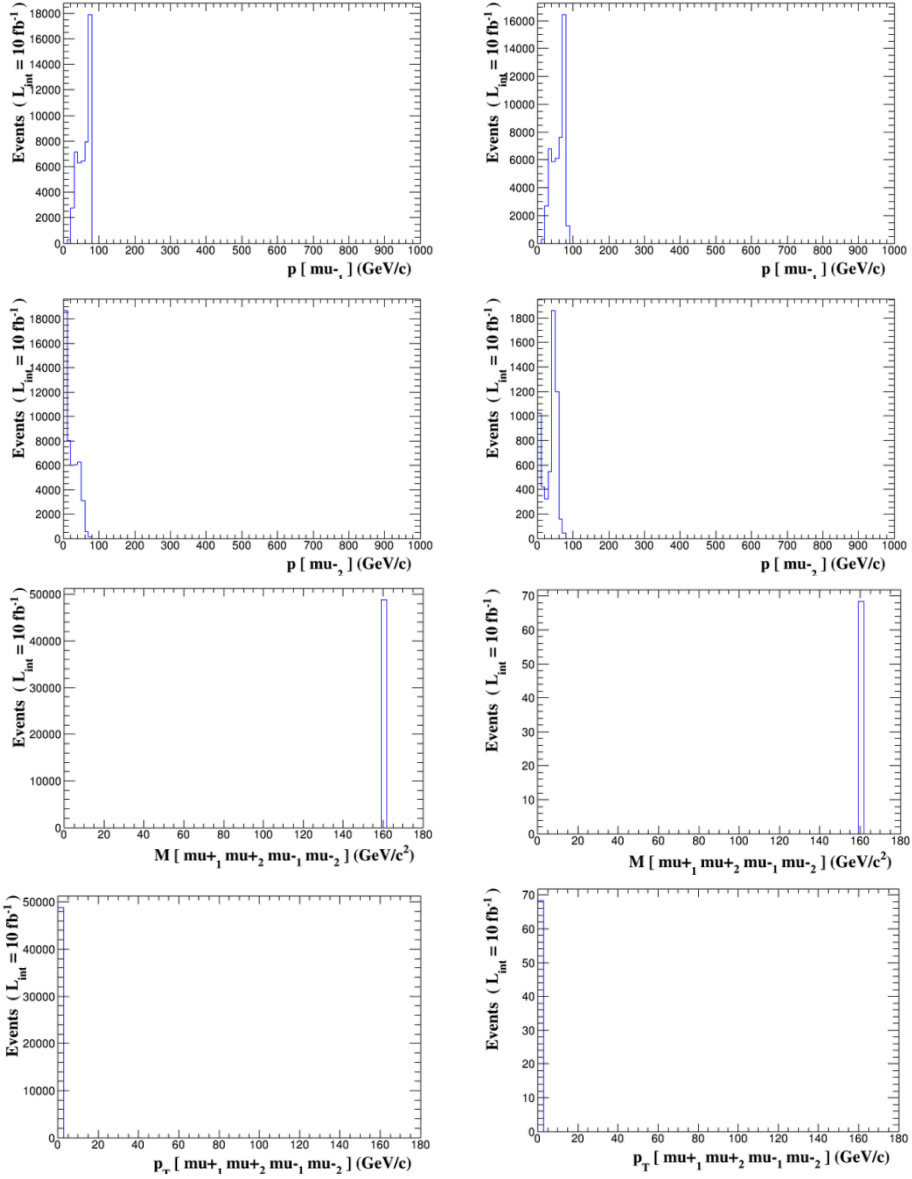


Figure 20. Comparison of generation level and reconstruction level at the FCC-ee (160 GeV). Number of events (y-axis) are multiplied by cross-section (4.88 pb) (continued).

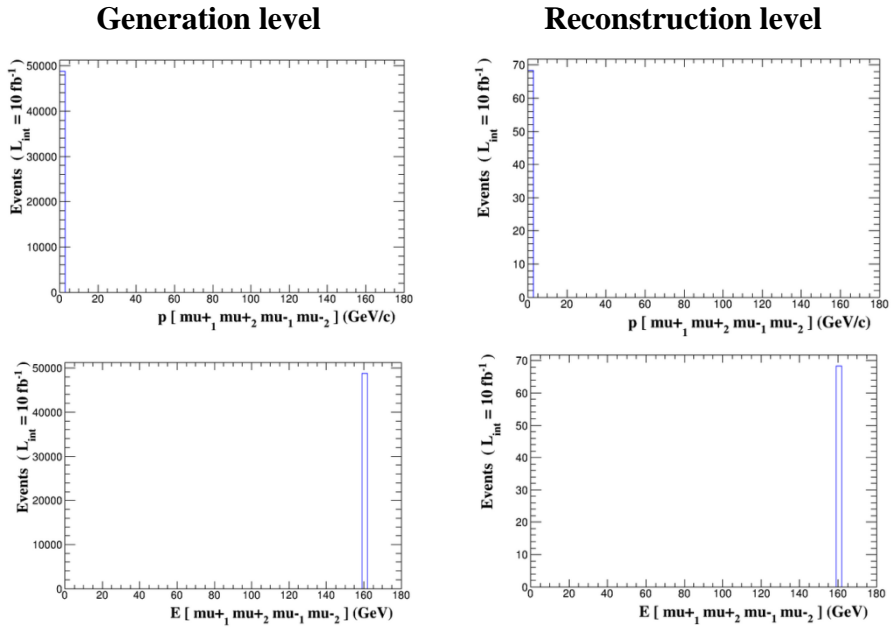


Figure 20. Comparison of generation level and reconstruction level at the FCC-ee (160 GeV). Number of events (y-axis) are multiplied by cross-section (4.88 pb) (continued).

[CEPC (160 GeV)]

Figure 21 shows the comparison of generation level and reconstruction level at the CEPC (160 GeV).

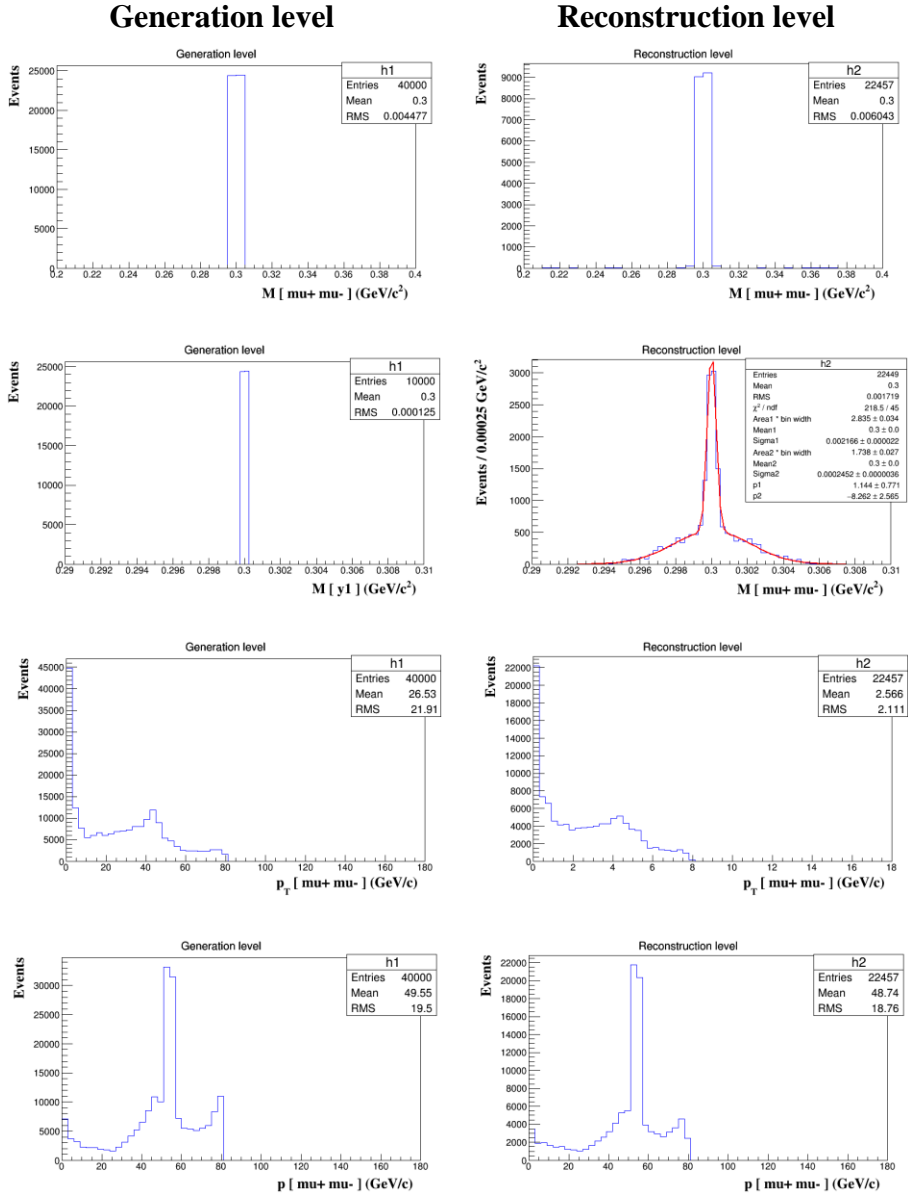


Figure 21. Comparison of generation level and reconstruction level at the CEPC (160 GeV). Number of events (y-axis) are multiplied by cross-section (4.88 pb).

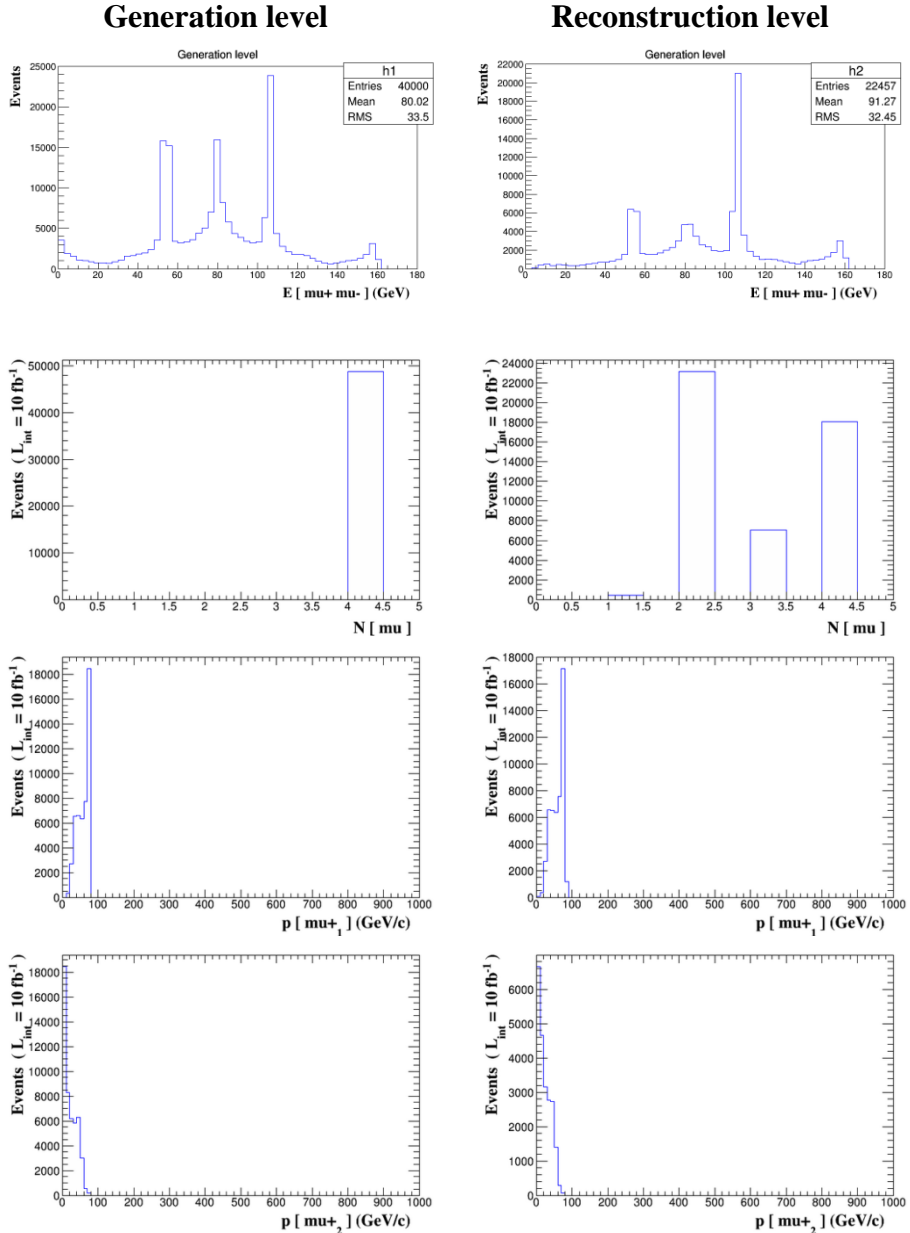


Figure 21. Comparison of generation level and reconstruction level at the CEPC (160 GeV). Number of events (y-axis) are multiplied by cross-section (4.88 pb) (continued).

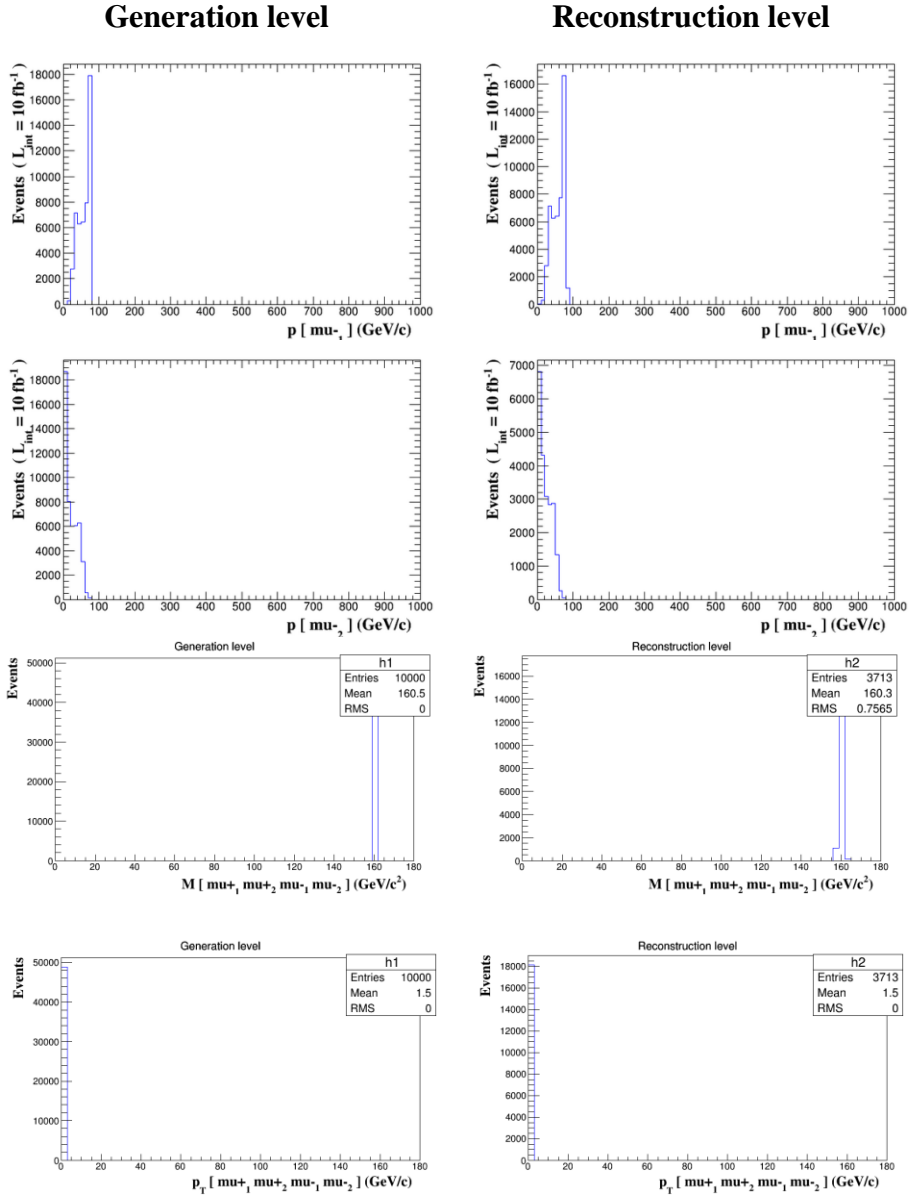


Figure 21. Comparison of generation level and reconstruction level at the CEPC (160 GeV). Number of events (y-axis) are multiplied by cross-section (4.88 pb) (continued).

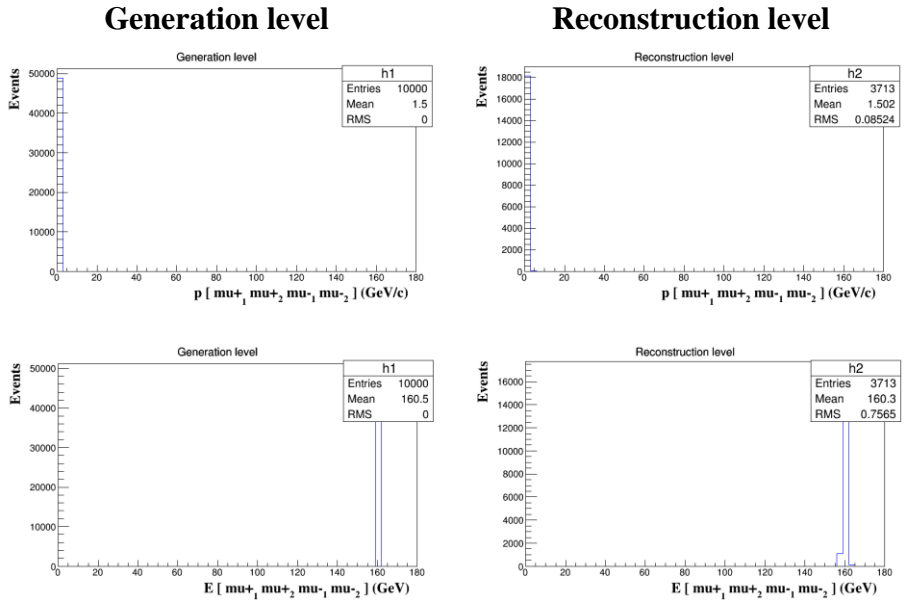


Figure 21. Comparison of generation level and reconstruction level at the CEPC (160 GeV). Number of events (y-axis) are multiplied by cross-section (4.88 pb) (continued).

[CEPC (240 GeV)]

Figure 22 shows the comparison of generation level and reconstruction level at the CEPC (240 GeV).

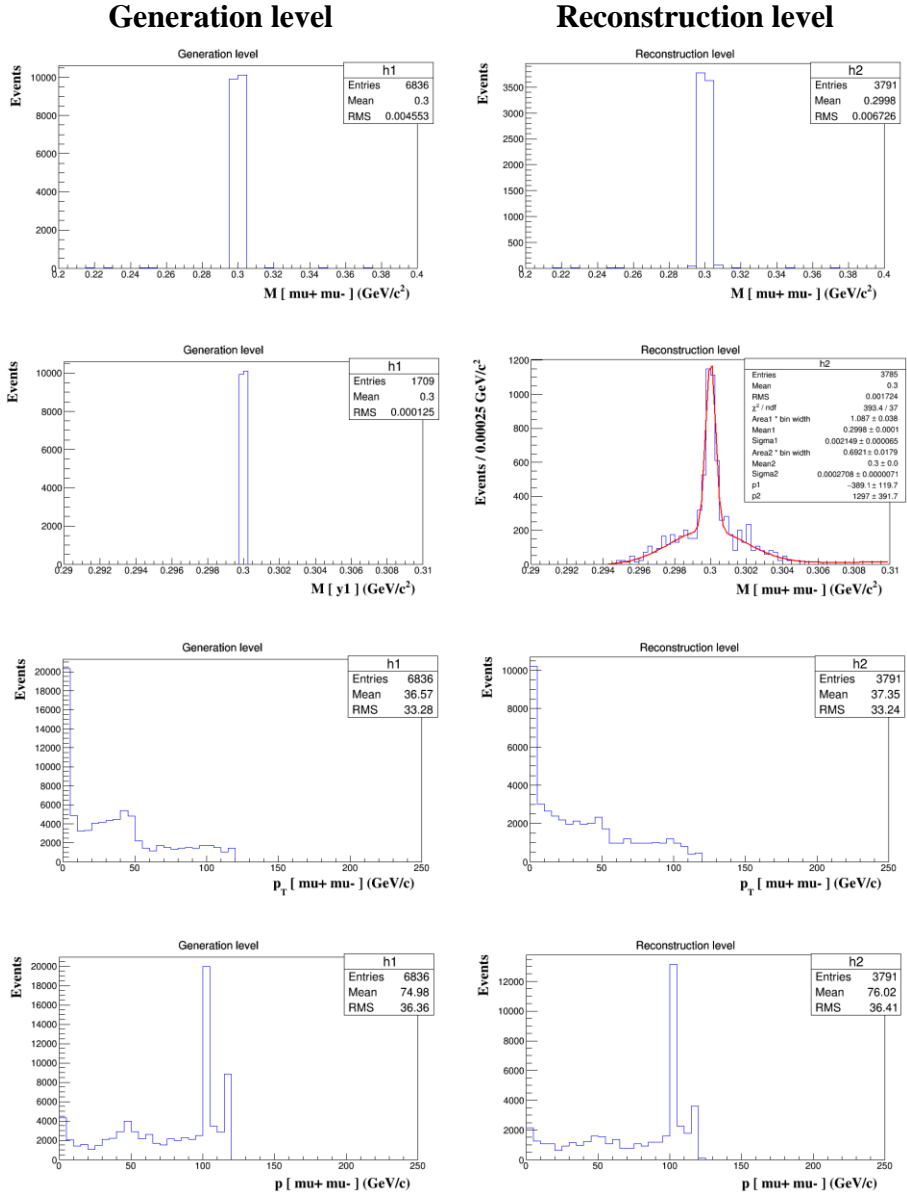


Figure 22. Comparison of generation level and reconstruction level at the CEPC (240 GeV). Number of events (y-axis) are multiplied by cross-section (2.0 pb).

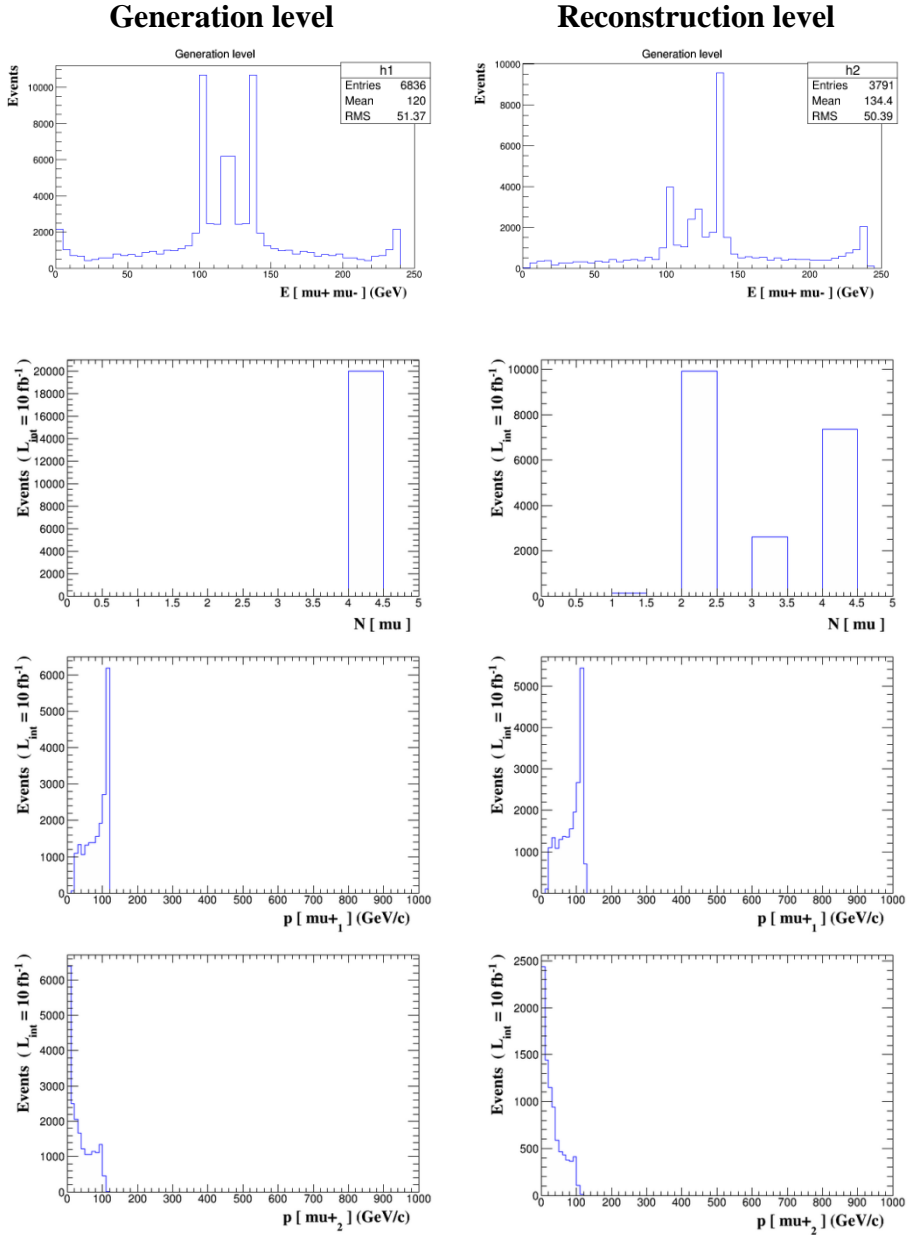


Figure 22. Comparison of generation level and reconstruction level at the CEPC (240 GeV). Number of events (y-axis) are multiplied by cross-section (2.0 pb) (continued).

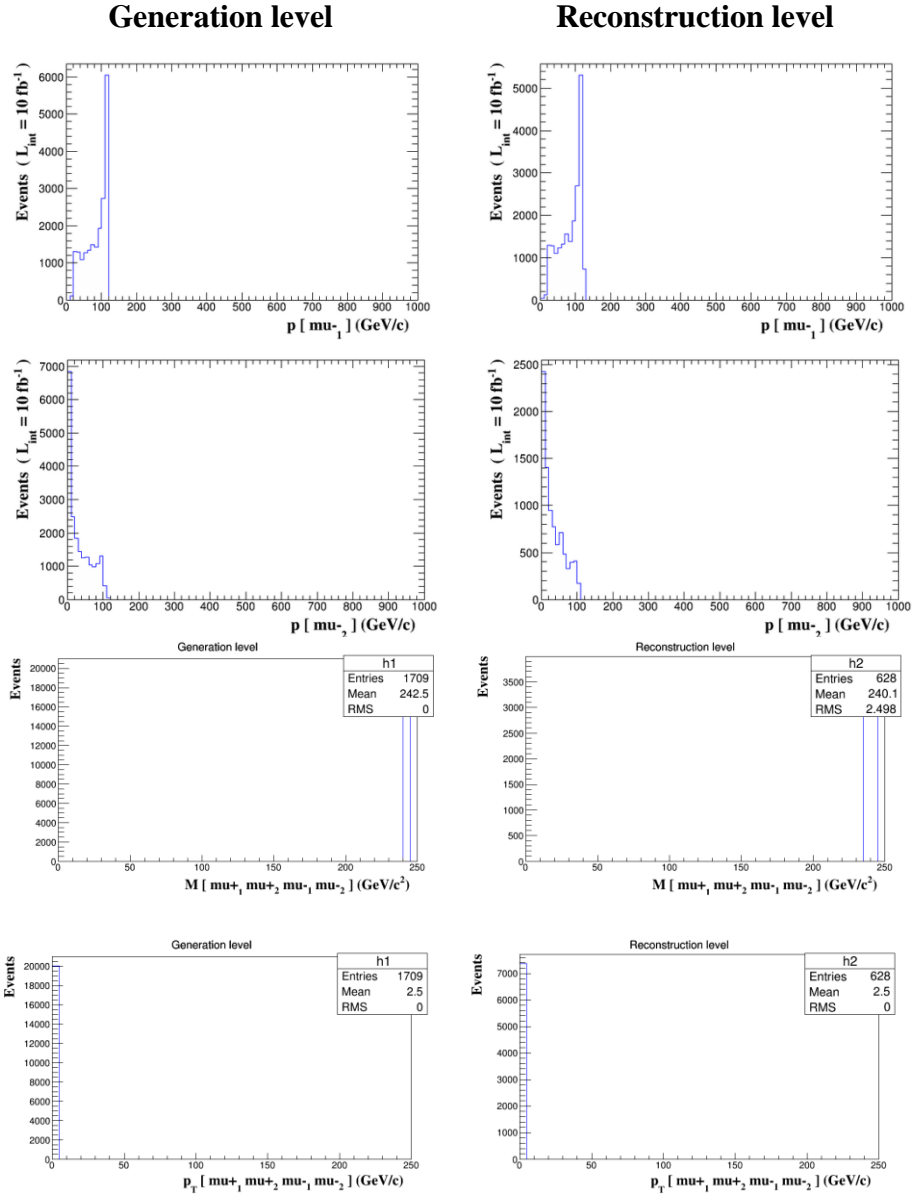


Figure 22. Comparison of generation level and reconstruction level at the CEPC (240 GeV). Number of events (y-axis) are multiplied by cross-section (2.0 pb) (continued).

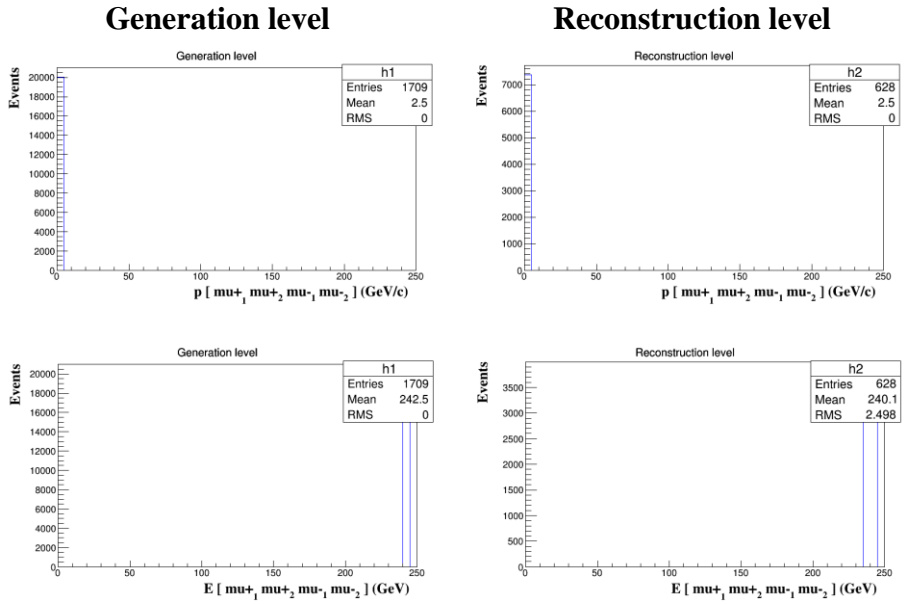


Figure 22. Comparison of generation level and reconstruction level at the CEPC (240 GeV). Number of events (y-axis) are multiplied by cross-section (2.0 pb) (continued).

[ILC (500 GeV)]

Figure 23 shows the comparison of generation level and reconstruction level at the ILC (500 GeV).

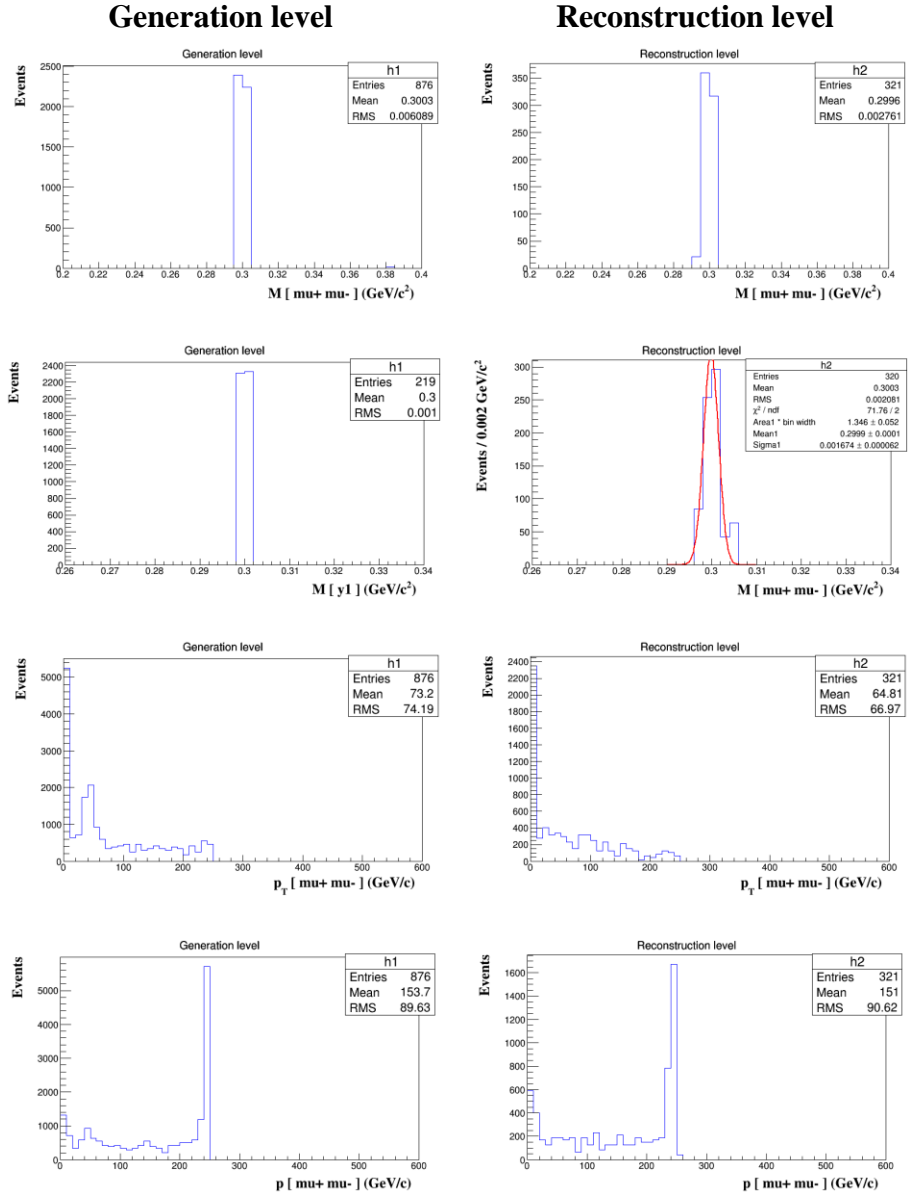


Figure 23. Comparison of generation level and reconstruction level at the ILC (500 GeV). Number of events (y-axis) are multiplied by cross-section (0.463 pb).

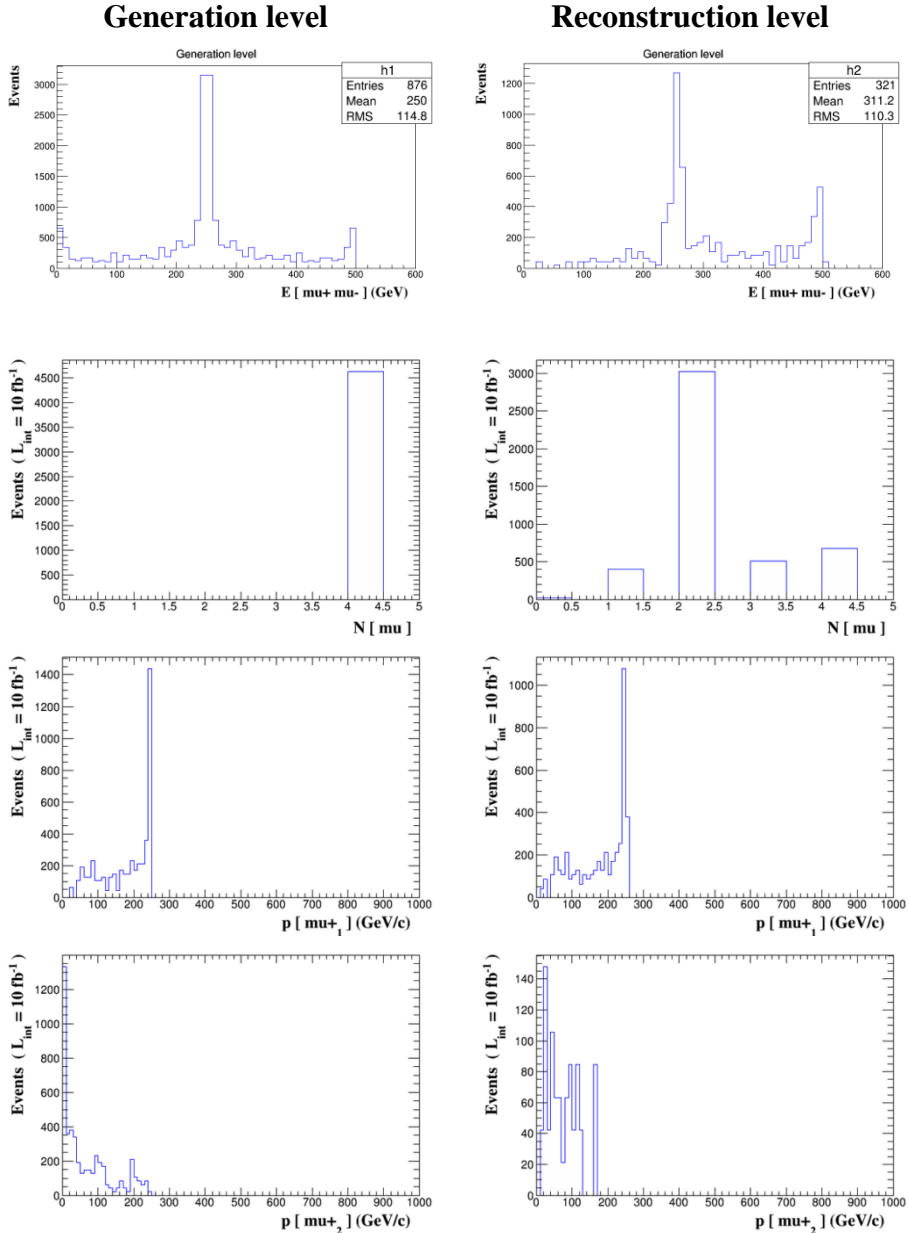


Figure 23. Comparison of generation level and reconstruction level at the ILC (500 GeV). Number of events (y-axis) are multiplied by cross-section (0.463 pb) (continued).

Generation level

Reconstruction level

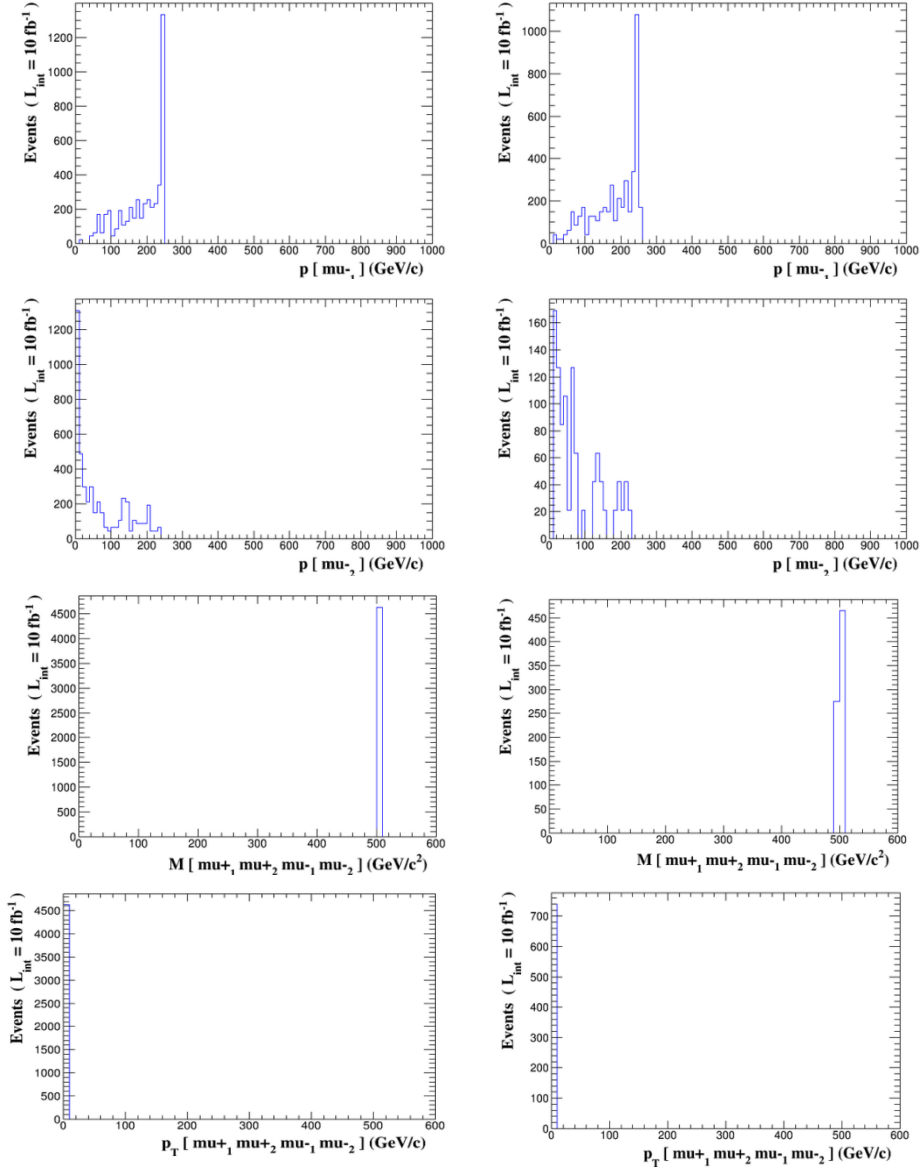


Figure 23. Comparison of generation level and reconstruction level at the ILC (500 GeV). Number of events (y-axis) are multiplied by cross-section (0.463 pb) (continued).

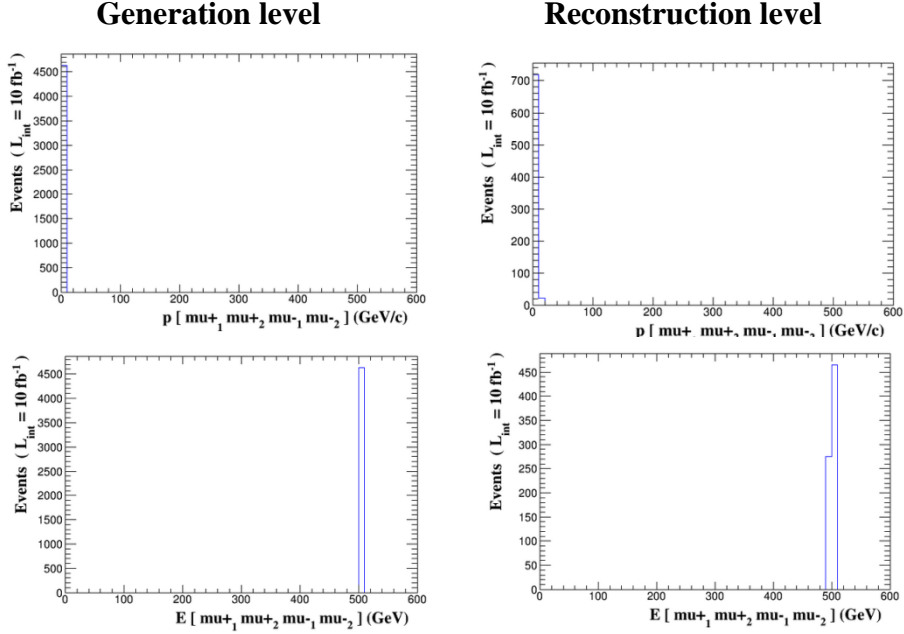


Figure 23. Comparison of generation level and reconstruction level at the ILC (500 GeV). Number of events (y-axis) are multiplied by cross-section (0.463 pb) (continued).

Table 13 and Figure 24 shows the detector acceptance of experiments. We can see that the CEPC has the highest detector acceptance. On the other hand, FCC-ee's detector acceptance was the lowest among experiments.

Table 13. Detector acceptance of experiments.

Experiments	CM energy [GeV]	Detector acceptance (%)
Belle II	10.58 GeV	11.325 ± 0.121
	(e^- : 7 GeV, e^+ : 4 GeV)	
FCC-ee	91 GeV	0.051 ± 0.000
	(e^\pm : 45.5 GeV)	
CEPC	160 GeV	37.484 ± 0.356
	(e^\pm : 80 GeV)	
CEPC	240 GeV	35.543 ± 0.839
	(e^\pm : 120 GeV)	
ILC	500 GeV	14.539 ± 0.562
	(e^\pm : 250 GeV)	

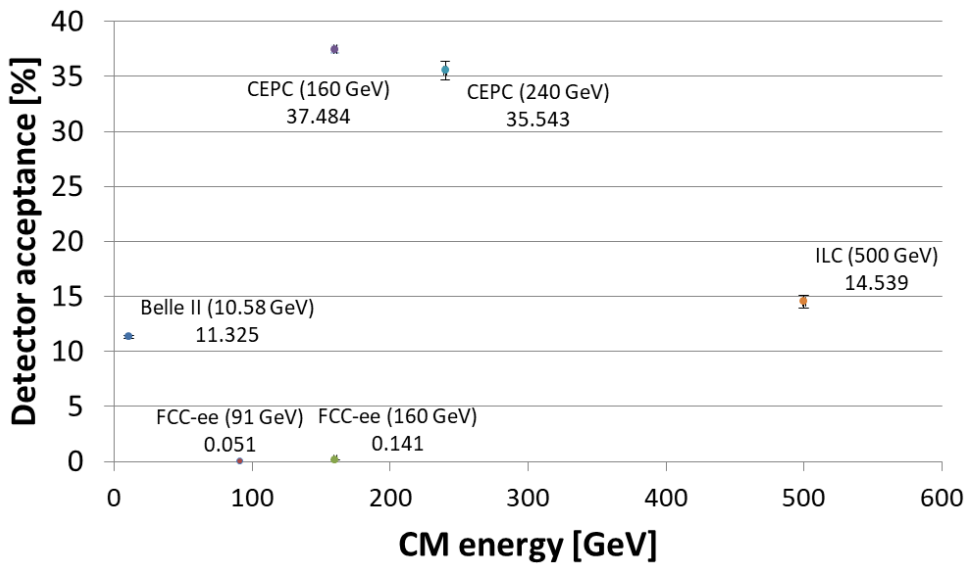


Figure 24. Detector acceptance of experiments.

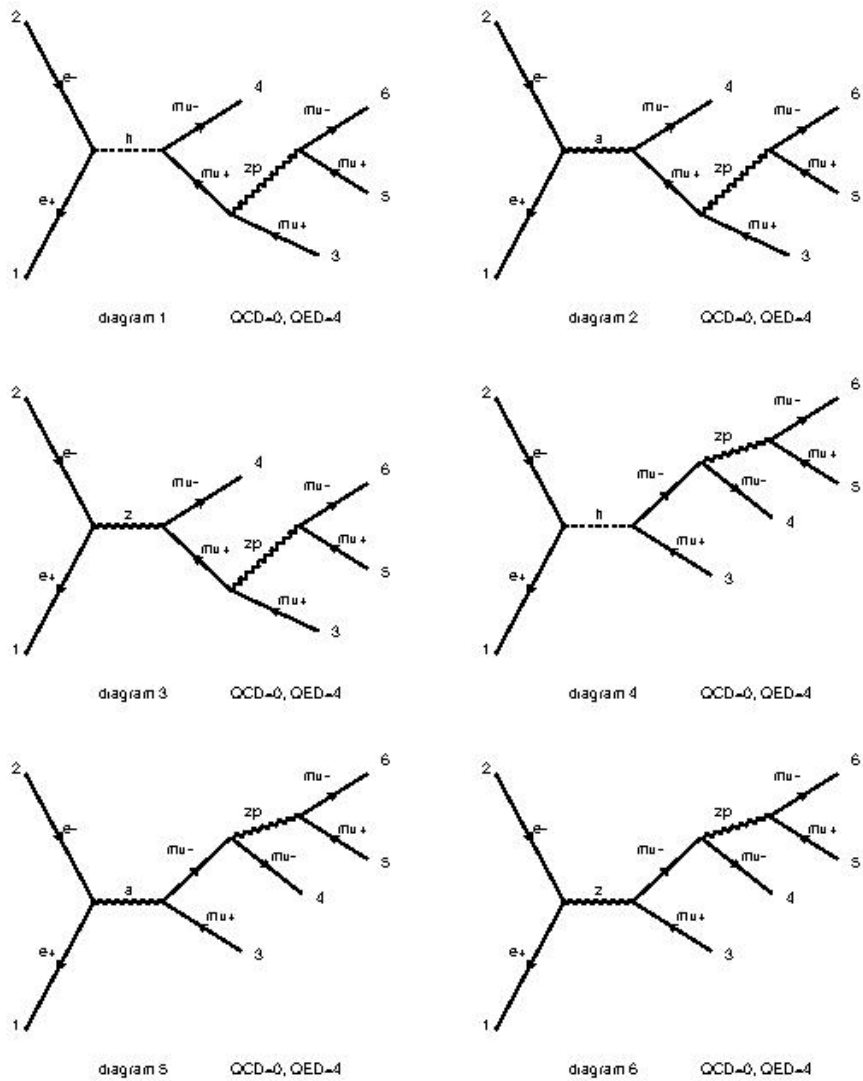
4.3 Signal channel studies based on the basf2

We have studied dark photon, which couples only to muons at CM energy of Belle II (10.58 GeV) based on the basf2. Table 14 shows the settings for the signal event generation based on the basf2. KEKCC work server and the basf2 were used for the study. The Zprime_Lmu_Ltau model was imported in MadGraph5 generating events. The number of events was 100,000. The CM energy was 10.58 GeV. The mass of dark photon was 0.3 GeV with the width, 6.7×10^{-6} GeV. The coupling constant was 0.1.

Table 14. The settings for the signal event generation based on the basf2.

Specification	Content
Machine	KEKCC work server
Software	basf2
Imported model	Zprime_Lmu_Ltau
Command for process	$e^+ e^- \rightarrow a, (a > \mu^+ \mu^- Z_p, Z_p > \mu^+ \mu^-)$
Number of events	100,000
CM energy	10.58 GeV
Mass of dark photon	0.3 GeV
(width)	$(6.7 \times 10^{-6} \text{ GeV})$
Coupling constant	0.1

Figure 25 shows that Feynman diagrams of the signal process. There are total 6 Feynman diagrams.



Diagrams made by MadGraph5_aMC@NLO

Figure 25. Feynman diagrams of the signal process.

We have compared physical quantities between in the generation level and in the reconstruction level using both the stand-alone frame and the basf2. We have compared invariant mass, transverse momentum, momentum, and energy of dark photon. Table 15 shows parameters and detector acceptance of the stand-alone frame and the basf2. As a result, detector is acceptance 11.325 ± 0.121 for the stand-alone frame and 0.915 ± 0.072 for the basf2.

Table 15. Parameters and detector acceptance of the stand-alone frame and the basf2.

	Stand-alone	basf2
Imported model	Simplified model	Zprime_Lmu_Ltau
Detector simulation	Delphes (CMS card)	Geant4
η cut	$-1.317 \leq \eta \leq 1.901$	
Command for process	$e^+ e^- \rightarrow a, (a \rightarrow \mu^+ \mu^- y1, y1 > \mu^+ \mu^-)$	$e^+ e^- \rightarrow a, (a \rightarrow \mu^+ \mu^- Zp, Zp > \mu^+ \mu^-)$
Number of events	10,000	100,000
CM energy	10.58 GeV	
Mass of dark photon	0.3 GeV	
(width)	$(6.7 \times 10^{-6} \text{ GeV})$	
Coupling constant	0.1	
Detector acceptance (%)	11.325 ± 0.121	0.915 ± 0.072

[Signal channel based on the stand-alone frame]

Figure 26 shows the comparison of generation level and reconstruction based on stand-alone frame.

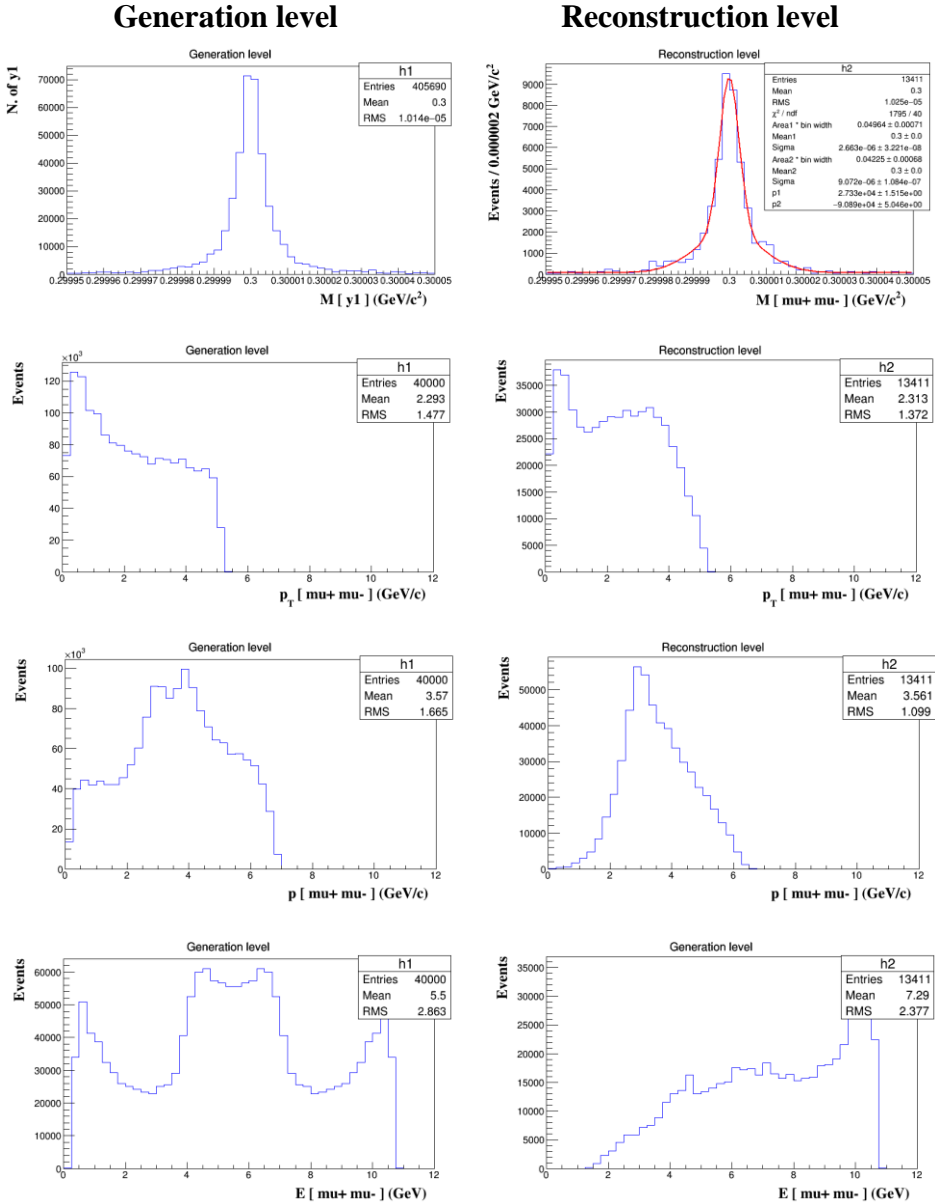


Figure 26. Comparison of generation level and reconstruction based on the stand-alone frame. Number of events (y-axis) are multiplied by cross-section (40.6 pb).

[Signal channel based on the basf2]

Figure 27 shows the comparison of generation level and reconstruction based on the basf2.

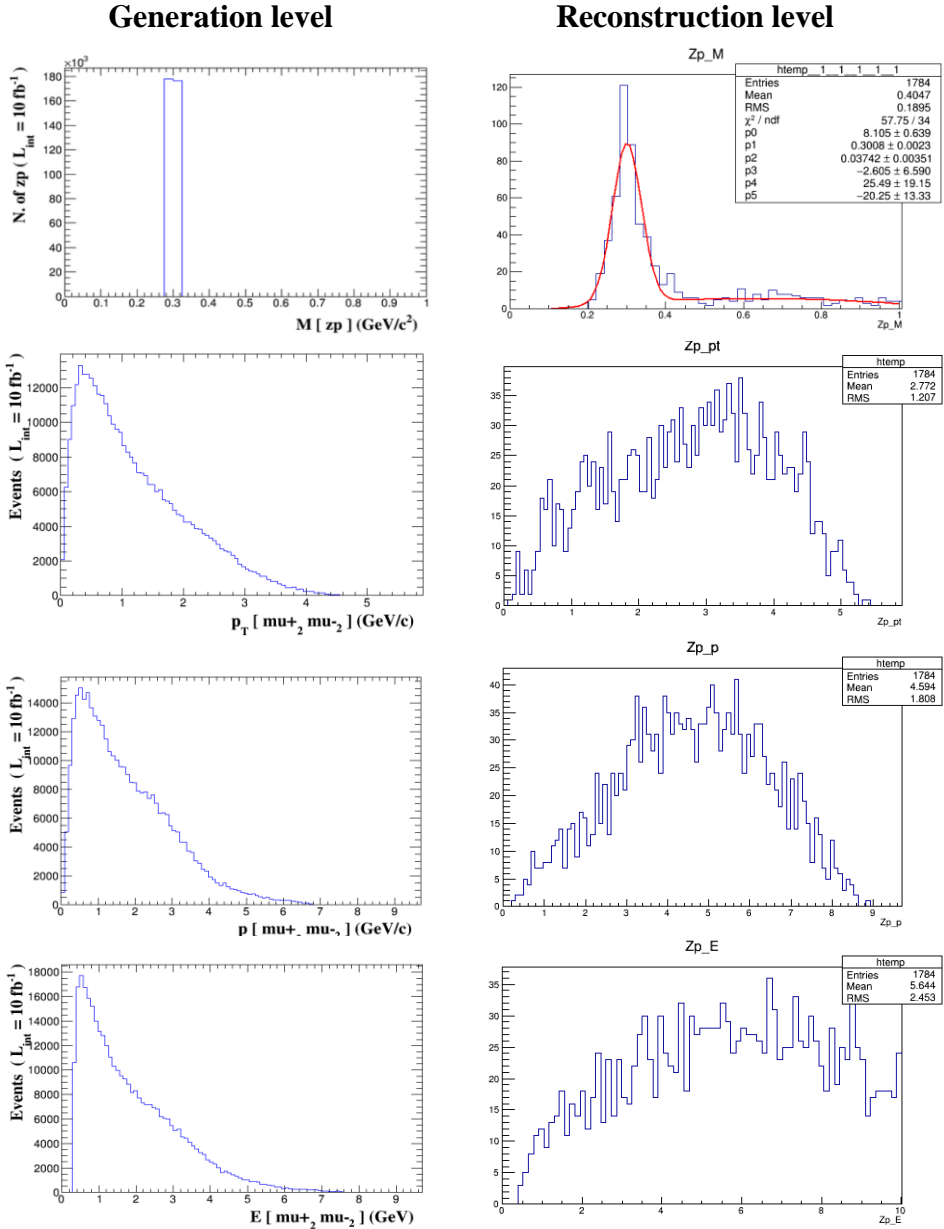


Figure 27. Comparison of generation level and reconstruction based on basf2. Number of events (y-axis) are multiplied by cross-section (35.4 pb).

4.4 CPU time studies on machines

The importance of computational science, which comprises theory, experiment, and simulation in science, have been emerging in the field of high energy physics (HEP), especially in searching for dark matter (Cho, K., 2016a; Cho, K., 2016b; Cho, K., 2017). Because the cross-section of dark matter is very tiny compared to that of the SM, a huge amount of calculation is required (Cho, K., 2017). Hence, reducing CPU time is important to increase the efficiency of research in HEP (Yeo, I., & Cho, K., 2020; Yeo, I., & Cho, K., 2019; Choi, W., Cho, K., & Yeo, I., 2018). We have used the KISTI-5 supercomputer (the KNL and the SKL) and the local Linux machine to compare wall-clock time of simulation. Table 16 shows the specification of the KISTI-5 supercomputer and the local Linux machine (Yeo, I., & Cho, K., 2020; Park, K., & Cho, K., 2021). The KNL and the SKL consist of 8305 and 132 nodes, with each node having 68 and 40 cores, respectively. The local Linux machine has 32 cores. The theoretical peak performance for the KISTI-5 supercomputer is 25.7 PFLOPS (with the KNL and the SKL corresponding to 25.3 and 0.4 PFLOPS, respectively) (Yeo, I., & Cho, K., 2020). Figure 28 shows the flowchart of physics and full simulation (Cho, K., 2016a; Cho, K., 2016b). First, physics simulation was performed using MadGraph5 (Alwall, J., et al., 2014) based on the simplified model (Alves, D., et al., 2012), and the event simulation was performed on the Pythia8 framework (Sjöstrand T., et al., 2015). Next, the detector simulation was performed using Delphes (Favereau, J. D., et al., 2014). Finally, reconstruction was performed using MadAnalysis5 (Conte, Fuks B., & Serret G., 2013).

Table 16. The specification of the KISTI-5 supercomputer and the local Linux machine.

Specification	KISTI-5 KNL	KISTI-5 SKL	Local Linux machine
OS	CentOS7.4	CentOS7.4	Scientific Linux 6.5
Processor	Intel Xeon Phi 7250 1.4 GHz	Intel Xeon Skylake (Gold 6148) 2.4 GHz	Intel Xeon CPU X5560 2.8 GHz
Architecture	Many-core	Multicore	Multicore
Number of cores/CPU	68	20	4
Number of CPUs/node	1	2	8
Number of cores/node	68	40	32
Number of total nodes	8,305	132	1
Number of total cores	564,740	5,280	32
Theoretical peak performance	25.3 PFLOPS	0.4 PFLOPS	-

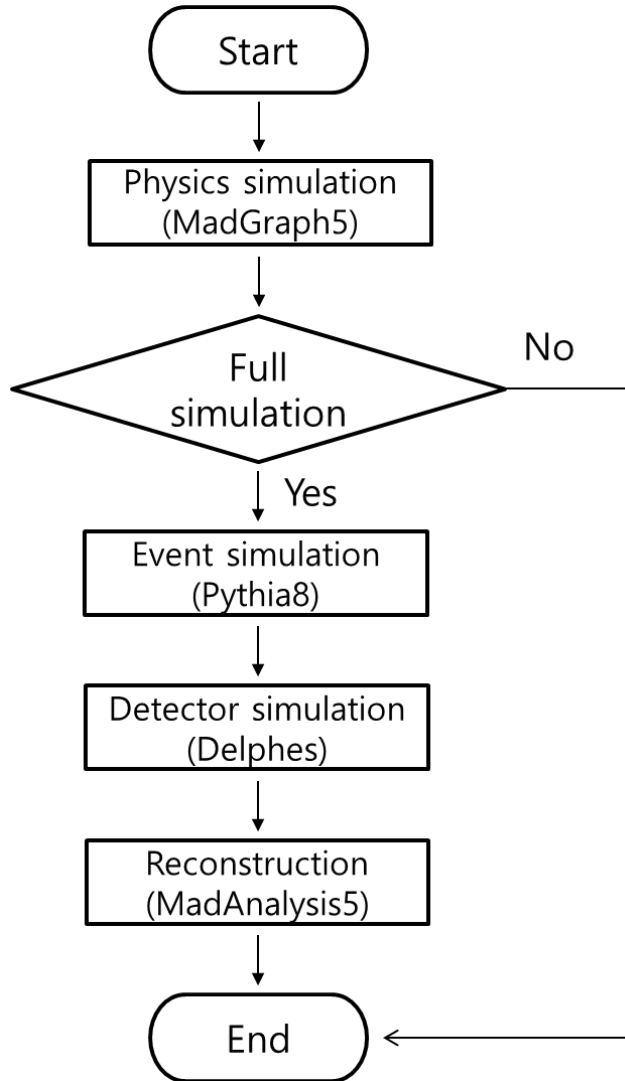


Figure 28. Flowchart of the physics and full simulation.

We have considered three cases in this study (Park, K., & Cho, K., 2021). In Case 1, only a physics simulation was considered. Case2 is the full simulation including not only physics simulation but also Pythia8, Delphes, and MadAnalysis5. Case3 is the examination of the efficiency of parallel processing depending on the number of jobs among the machines. Table 17 describes the

configuration of three cases: physics simulation only, full simulation, and physics simulation with parallel processing. For all three cases, a simplified model was used, and the signal process was $e^+ e^- \rightarrow \gamma \rightarrow \mu^+ \mu^- A'$ with $A' \rightarrow \mu^+ \mu^-$. The mass of dark photon was 0.3 GeV with the width, 6.7×10^{-6} GeV. The number of events was 10,000. The CM energy was 10.58 GeV (7 and 4 GeV for the electron and positron, respectively). The coupling constant was 0.1.

Table 17. The configuration for the three cases.

Item	Case 1	Case 2	Case 3	
	Physics simulation only	Full simulation	Physics simulation only with parallel processing	
Dark photon mass [GeV]	0.3	0.3	0.3	
(width [GeV])	(6.7×10^{-6})	(6.7×10^{-6})	(6.7×10^{-6})	
Physics simulation (MadGraph5 v2.6.4)	On	On	On	
Pythia8, Delphes (CMS), MadAnalysis5	Off	On	Off	
No. of jobs	KNL	15	1, 3, 6, ..., 60, 63, 66	
			SKL	1, 3, 6, ..., 27, 30, 33
				Local machine
Iteration	1	1	10	

In Case 1, for the physics simulation only, events were generated using MadGraph5. 15 jobs were submitted to be performed through parallel processing across all three machines. Figure 29 shows the results of the wall-clock time when using the KNL, the SKL, and the local Linux machine. One core was used to determine the wall-clock time. Moreover, one node (68, 40, and 32 cores for the KNL, the SKL, and the local Linux machine, respectively) was used to determine the wall-clock time. For a single core, it was noted that the wall-clock time of the SKL was faster than that of the KNL and the local Linux machine by a factor of 4.9 and 4.3, respectively. Compared to the one core case, the wall-clock time of one node (multiple cores) of the KNL, the SKL, and the local Linux machine was reduced by a factor of 6.8, 5.3, and 1.4, respectively. In wall-clock time of one node, the computation time of the SKL was 3.8 times faster than the KNL and 16 times faster than the local Linux machine. This result indicates that the efficiency of parallel processing for 15 jobs of the KISITI-5 supercomputer (the KNL and the SKL) was higher than that of the local Linux machine. Figure 30 shows the speed up on machines and the ideal case. The speed up was obtained by dividing the wall-clock time of sequential calculations by the wall-clock time of parallel calculations. In the ideal case of 15 jobs, speed up would be 15. When the number of jobs is 15, the KNL's speed up was the highest speed-up among the three machines.

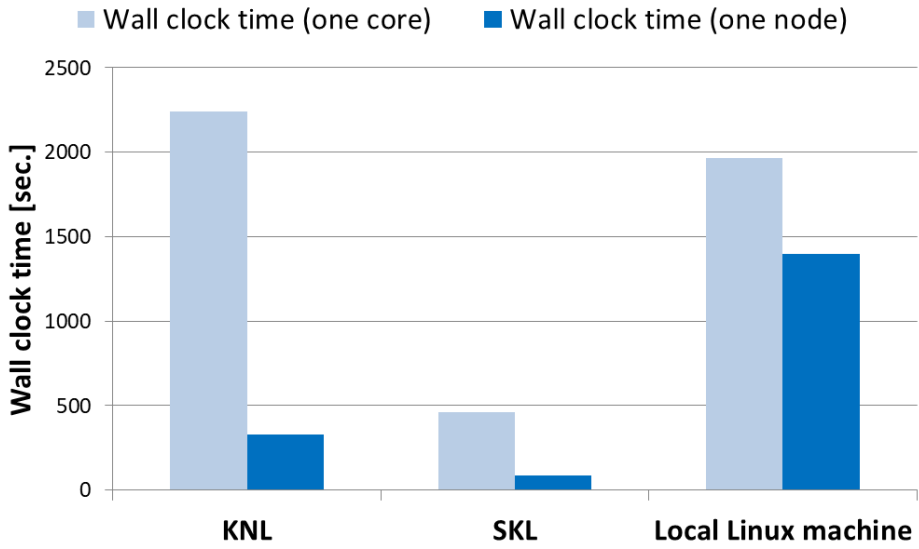


Figure 29. Wall-clock time with one core or 15 cores on machines with physics simulation only.

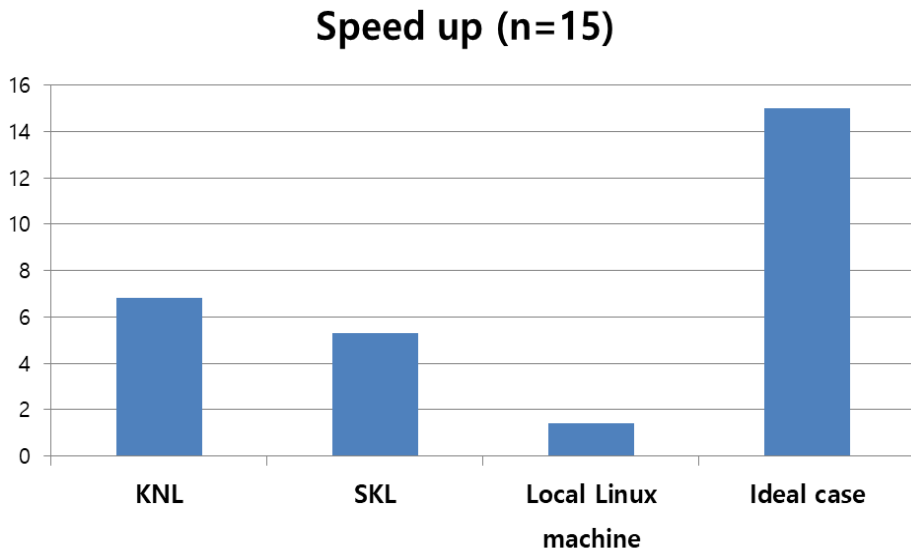


Figure 30. Speed up on machines and ideal case.

In Case 2, for the full simulation, Pythia8, Delphes, and MadAnalysis5 software were employed. 15 jobs were calculated using one core (serial processing). Figure 31 shows the wall-clock time on the KNL, the SKL, and the local Linux machine for the full simulation. Compared to physics simulation only, the full simulation was faster, with the following order: SKL > local Linux machine \gtrsim KNL. The calculation time for the SKL was 5.5 times faster than the KNL and 5.3 times faster than the local Linux machine.

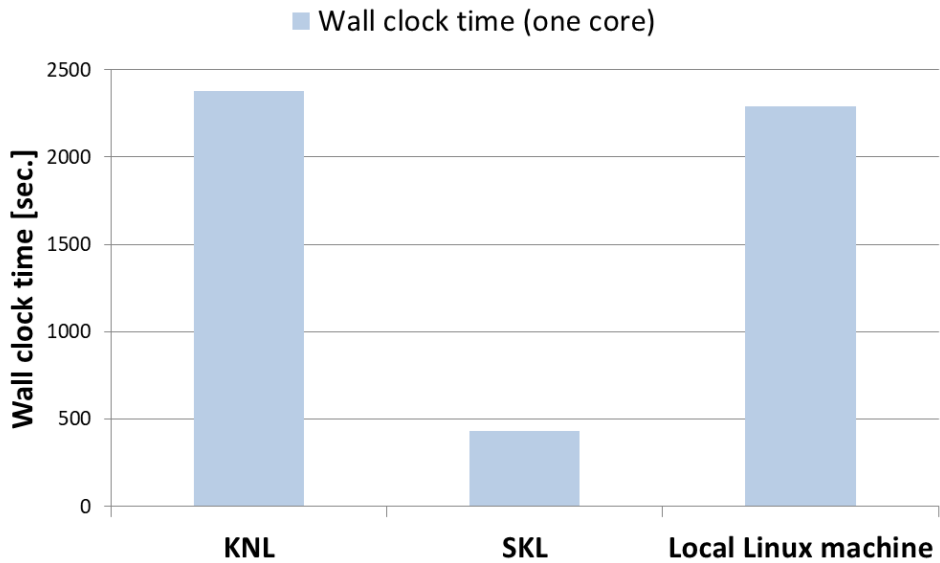


Figure 31. Wall-clock time with one core on machines with the full simulation.

In Case3, we have examined the efficiencies of parallel processing depending on number of jobs among machines. We have performed physics simulation only. We have repeated this processing 10 times in order to reduce statistical error. Figure 32 shows the wall-clock time as the number of job increases for different machines. The plotted data are the average values obtained from 10 individual processing using each machine. The higher efficiency of parallel processing corresponded to a smaller slope. In the ideal case, the slope is expected to be zero for the highest efficiency of parallel processing. The efficiency of parallel processing was 4.1 and 22 times higher than that of the KNL and local Linux machine, respectively. This result shows that although the performance of one core of the KNL was lower than that of the local Linux machine, the efficiency of parallel processing with a large number of the KNL cores was higher than that for the local Linux machine.

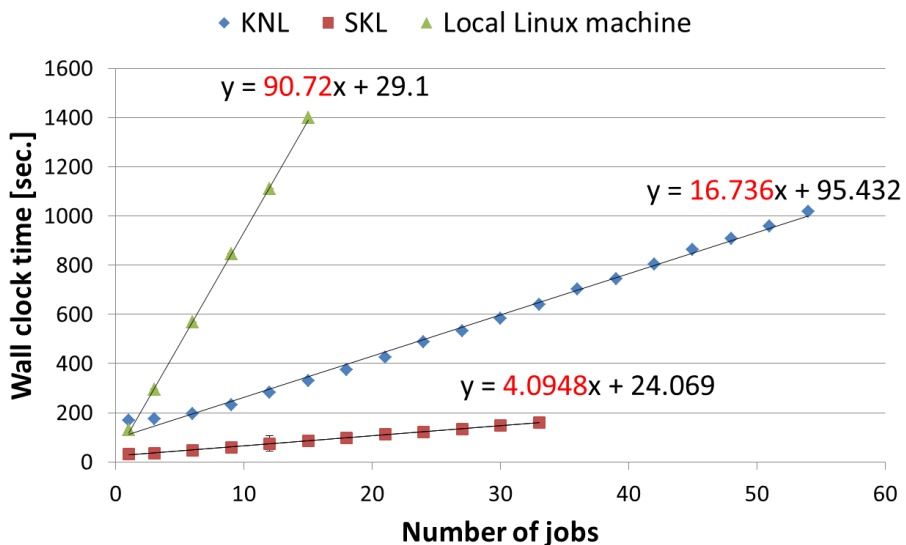


Figure 32. Wall-clock time as the number of jobs increases for different machines.

5. Conclusion

Using HEP simulation tool kits, we have studied dark matter at electron-positron colliders. At the generation level, cross-section according to various parameters such as CM energy, mass of dark photon (A'), and coupling constant was studied. When the CM energy was 90 GeV, the peak of the cross-section was observed around the mass of Z boson. At the reconstruction level, we obtained detector acceptance of present and/or future electron-positron collider experiments. Among the experiments, the CEPC had the highest detector acceptance of about 37 percent while the FCC-ee had the lowest detector efficiency of less than 1 percent. At the CM energy of Belle II (10.58 GeV), we have also used the basf2, which utilize the Geant4 for full detector simulation. We have compared invariant mass, transverse momentum, momentum, and energy of dark photon based on the stand-alone frame and the basf2. These results will help to search for dark matter in present and/or future electron-positron experiments. In addition, we used the KISTI-5 supercomputer (the KNL and the SKL) and the local Linux machine with one or more cores to compare the CPU time. The wall-clock time of one node taken by the SKL was 3.8 times faster than the KNL and 16 times faster than the local Linux machine. For the dependence of the efficiency of parallel processing on the number of jobs, the SKL was 4.1 times higher than the KNL and 22 times higher than the local Linux machine. The results show that utilizing numerous cores in supercomputers can help in significantly reducing the computation time of HEP simulations. This in turn will help in optimizing the HEP software using high performance computing.

Bibliography

- Alves, D., et al. (2012), ‘Simplified models for LHC new physics searches’, *J. Phys. G: Nucl. Part. Phys.*, 39, 105005. <http://dx.doi.org/10.1088/0954-3899/39/10/105005>
- Alwall, J., et al. (2014), ‘The automated computation of tree-level and next-to-leading order differential cross sections, and their matching to parton shower simulations’, *J. High Energ. Phys.* 79. [https://doi.org/10.1007/JHEP07\(2014\)079](https://doi.org/10.1007/JHEP07(2014)079)
- Antcheva, I., et al. (2009), ‘Root—A C++ framework for petabyte data storage, statistical analysis and visualization’, *Comp. Phys. Comm.*, 180, 2499–2512. <https://doi.org/10.1016/j.cpc.2009.08.005>
- Cho, K. (2016a), ‘e-Science Paradigm for Astroparticle Physics at KISTI’, *J. Astron. Space Sci.*, 33, 63–67. <https://doi.org/10.5140/JASS.2016.33.1.63>
- Cho, K. (2016b), ‘Computational science and the search for dark matter, New Phys. Sae Mulli’, 66, 950–956. <https://doi.org/10.3938/NPSM.66.950>
- Cho, K. (2017), ‘Computational science-based research on dark matter at KISTI’, *J. Astron. Space Sci.*, 34(2), 153–159. <https://doi.org/10.5140/JASS.2017.34.2.153>
- Choi, W., Cho, K., & Yeo, I. (2018), ‘Performance profiling for brachytherapy applications’, *Comp. Phys. Comm.*, 226, 180–186. <https://doi.org/10.1016/j.cpc.2017.12.022>
- Conte, Fuks B., & Serret G. (2013), ‘Madanalysis 5, a user-friendly framework

- for collider phenomenology’, *Comp. Phys. Comm.*, 184, 222–256.
<https://doi.org/10.1016/j.cpc.2012.09.009>
- Favereau, J. D., et al. (2014), ‘Delphes 3: a modular framework for fast simulation of a generic collider experiment’, *J. High Energ. Phys.*, 523, 3-4. [https://doi.org/10.1007/JHEP02\(2014\)057](https://doi.org/10.1007/JHEP02(2014)057)
- Park, K., & Cho, K. (2021), ‘A Study of Dark Photon at the Electron-Positron Collider Experiments Using KISTI-5 Supercomputer’, *J. Astron. Space Sci.*, 38(1), 55-63. <https://doi.org/10.5140/JASS.2021.38.1.55>
- Shuve, B., & Yavin, I. (2014), ‘Dark matter progenitor: Light vector boson decay into sterile neutrinos’, *Phys. Rev. D*, 89, 113004.
<https://doi.org/10.1103/PhysRevD.89.113004>
- Sjöstrand T., et al. (2015), ‘An introduction to PYTHIA 8.2’, *Comp. Phys. Comm.*, 191, 159–177. <https://doi.org/10.1016/j.cpc.2015.01.024>
- Yeo, I., & Cho, K. (2018), ‘Researches on dark matter using e+ e- collider’, *J. Astron. Space Sci.*, 35, 67–74. <https://doi.org/10.5140/JASS.2018.35.2.67>
- Yeo, I., & Cho, K. (2019), ‘Study on geant4 simulation toolkit using a low energy physics profiling system’, *J. Korean Phys. Soc.*, 74, 923–929.
<https://doi.org/10.3938/jkps.74.923>
- Yeo, I., & Cho, K. (2020), ‘Low-energy physics profiling of the geant4 simulation tool kit on evolving computing architectures’, *J. Korean Phys. Soc.*, 76, 1047–1053. <https://doi.org/10.3938/jkps.76.1047>
- Zyla, P. A., et al. (2020), ‘Particle Data Group’, *Prog. Theor. Exp. Phys.* 2020, 083C01

사사(謝辭)

UST-KISTI 캠퍼스에서 데이터 및 HPC 과학 석사과정 학위를 수여하기까지 2 년이라는 길고도 짧은 시간이 지났습니다. 많이 부족한 제가 석사과정을 무사히 마칠 수 있었던 것은 KISTI 캠퍼스에서 만난 소중하고 고마운 분들이 있었기에 가능했습니다.

먼저, 지도교수님이신 조기현 교수님께 가장 큰 감사의 말씀을 전하고 싶습니다. 교수님의 헌신적인 지도와 격려 덕분에 부족함 없이 학업과 연구에 집중하여 좋은 결과를 얻을 수 있었습니다. 아낌없이 주신 학업적 개인적 조언 덕분에 석사과정 동안 많은 경험과 지식을 쌓을 수 있었습니다.

또한 석사학위논문 심사위원회로 참여하시어 귀중한 조언으로 논문의 완성도를 높이는데 큰 도움을 주신 정민중 교수님(센터장님), 이홍석 교수님께 감사의 말씀 드립니다.

또한 고에너지물리연구팀에 함께 있으면서 여러가지 학업적 조언과 유용한 피드백을 주신 여인성 박사님, 문명환 박사님께도 감사의 말씀을 드립니다.

병렬컴퓨팅에 관련하여 많은 조언을 주신 권오경 박사님, 윤태호 박사님께 감사의 말씀 드립니다.

좋은 연구 환경을 조성해주시고 다양한 세미나, 학회 및 워크숍에 참가할 수 있는 기회를 주신 염민선 전 센터장님을 비롯한 KISTI 슈퍼컴퓨팅응용센터의 모든 분들에게도 감사 드립니다.

UST 학생들이 더 나은 환경에서 학업과 연구를 수행할 수 있게 항상 노력해주시고 많은 도움을 주신 조금원 캠퍼스 대표 교수님(전 부원장님), 황순욱 전공 대표 교수님(전 본부장님)께도 깊은 감사를 드립니다.

또한 학업적으로 조언을 주시고 외적으로도 신경 써주시는 김홍서 교수님께 감사를 드립니다.

많은 시간을 함께하며 저의 대학원 생활에 큰 힘이 되어준 나혜인, 양동현 학생에게 고마움을 전합니다. 특히, 석사과정 동안 큰 힘이 되어준 최익제, 윤영미, Mai Ngoc Kien 동기들에게 감사를 드립니다. 병렬처리 연구에 많은 도움을 주고 항상 솔선수범하여 학생들을 위해 다방면으로 노력해준 유찬희 학생 조교에게 고마움을 전합니다. 또한 학생들을 위하여 여러 가지로 수고해주는 공병윤 학생대표에게도 감사의 말을 전합니다. 학생연구실에서 오랫동안 같은 시간을 보낸 Athita Onuean, Chirawan Ronran, Inayat Ali, 이창무, 이지연, 김유선, 이건호, 유주연 학생에게 고마움을 전합니다. KISTI 캠퍼스에 적응하는데 많은 도움을 준 진승교 석사, 임동진 석사, 박수현 학생, 김호용 석사에게도 고마움을 전합니다.

비록 논문을 쓰는 데 직접적인 도움을 주지는 않았지만 정신적으로 큰 도움을 준 친구들인 김지웅, 류동완, 박동빈, 서우열에게도 감사하다는 말을 전합니다.

또한, 제가 학업에 매진할 수 있도록 뒤에서 늘 힘이 되어 주시는 어머니와 가족들에게 깊은 감사의 말씀을 드립니다. 항상 저를 믿어주시고 힘이 되어주셔서 감사합니다.

이외에도 저에게 도움을 주신 많은 분들이 계십니다. 그 분들의 존함을 모두 거론하며 한 분 한 분 감사를 드려야 하는 것이 도리어오나, 지면의 한계로 신지 못하는 점에 대해 너그러이 용서해 주시기 바랍니다.

모든 분들의 행복을 기원합니다.

2021 년 8 월

박기홍 올림